Noncanonical roles of ATG5 and membrane atg8ylation in retromer assembly and function

Masroor Ahmad Paddar[1,2], Fulong Wang[1,2], Einar S Trosdal[1,2], Emily Hendrix[3], Yi He[3], Michelle Salemi[4], Michal Mudd[1,2], Jingyue Jia[1,2], Thabata L A Duque[1,2], Ruheena Javed[1,2], Brett Phinney[4], and Vojo Deretic[1,2,5]*

[1]Autophagy, Inflammation and Metabolism Center of Biochemical Research Excellence.
[2]Department of Molecular Genetics and Microbiology, University of New Mexico School of Medicine, 915 Camino de Salud, NE, Albuquerque, NM 87131, USA.
[3]Department of Chemistry & Chemical Biology, The University of New Mexico, Albuquerque, NM, USA.
[4]Proteomics Core Facility, UC Davis Genome Center, University of California, Davis, CA 95616, USA.
[5]Lead Contact

*Correspondence:
Vojo Deretic, Ph.D.
Department of Molecular Genetics and Microbiology
University of New Mexico Health Sciences Center
915 Camino de Salud, NE
Albuquerque, NM 87131
U.S.A.
vderetic@salud.unm.edu

ABSTRACT

ATG5 is one of the core autophagy proteins with additional functions such as noncanonical membrane atg8ylation, which among a growing number of biological outputs includes control of tuberculosis in animal models. Here we show that ATG5 associates with retromer's core components VPS26, VPS29 and VPS35 and modulates retromer function. Knockout of ATG5 blocked trafficking of a key glucose transporter sorted by the retromer, GLUT1, to the plasma membrane. Knockouts of other genes essential for membrane atg8ylation, of which ATG5 is a component, affected GLUT1 sorting, indicating that membrane atg8ylation as a process affects retromer function and endosomal sorting. The contribution of membrane atg8ylation to retromer function in GLUT1 sorting was independent of canonical autophagy. These findings expand the scope of membrane atg8ylation to specific sorting processes in the cell dependent on the retromer and its known interactors.

INTRODUCTION

The canonical autophagy pathway, ubiquitous in eukaryotes, is manifested by the emergence of intracellular membranous organelles termed autophagosomes that capture cytoplasmic cargo destined for degradation in lysosomes [1]. Progress has been made in understanding molecular mechanisms governing canonical autophagosome biogenesis in mammalian cells [2] including ATG9A-vesicles [3-7] and membranous prophagophores [8] as precursors to LC3-positive phagophores, their reshaping as cups [9] and dynamic interactions with the omegasomes [10,11], phagophore expansion through lipid transfer [12-14], cargo recognition and sequestration [15,16], closure of the phagophore to form a double membrane phagosomes [17-20], and fusion of autophagosomes with endosomal and lysosomal organelles leading to cargo degradation [21] or secretion [22].

However, and contemporaneously with these major advances in understanding canonical autophagy, it has become evident that autophagy genes (ATGs) [23] have additional functions in mammalian cells that do not fit the canonical model [24,25]. Among such noncanonical manifestations are LAP (LC3-associated phagocytosis) [26], LANDO (LC3-associated endocytosis) [27], LC3-associated micropinocytosis (LAM) [28], conjugation of ATG8 to single membranes (CASM) [29,30], v-ATPase-ATG16L1-induced LC3 lipidation (VAIL) [31-33], ER-phagy mediated by the V-ATPase-ATG16L1-LC3C axis (EVAC) [34], LyHYP (lysosomal hypersensitivity phenotype) [35], membrane damage repair [36-39], and two distinct forms of secretory autophagy [22], SALI (secretory autophagy during lysosome inhibition) [40] and LDELS (LC3-dependent EV loading and secretion) [41]. These processes depend on or are associated with the phospholipid conjugation cascade of mammalian ATG8 proteins (mATG8s) [42] and collectively (including the canonical autophagy) represent diverse manifestations of membrane atg8ylation as a broad membrane stress, damage and remodeling response [25].

The factors governing membrane atg8ylation include two enzymatic cascades with the ATG12-ATG5 and mATG8-phosphatidylethanolamine (PE) covalent conjugates as their products. The ATG12-ATG5 conjugate [42] combines with ATG16L1 [43] or TECPR1 to form E3 ligases [38,39,44] to direct mATG8-PE conjugation and atg8ylation of

target membranes. All known E3 enzymes contain the ATG12-ATG5 conjugate [38,39,42,44]. To form this conjugate, the ubiquitin like molecule ATG12 is activated by ATP, and transferred via E1 (ATG7) and E2 (ATG10) to ATG5. In preparation for the next step, an ATG12-ATG5 containing E3 ligase activates its substrate mATG8-ATG3 to transfer ATG8 and form an amide bond with aminophospholipids [42]. However, there are additional branches of these conjugation cascades, whereby ATG12 can make a noncanonical sidestep conjugate with ATG3 (ATG12-ATG3) [41,45] which is enhanced in the absence of ATG5 [35]. Apart from its role in atg8ylation, ATG5 [35,46] and potentially other ATG genes [47-49] have autophagy-independent functions. Many of the indications that such functions exist come from in vivo studies [50-52]. For example, in the case of murine models of *Mycobacterium tuberculosis* infection, atg8ylation machinery protects against tuberculosis pathogenesis but Atg5 knockout has a particularly strong phenotype exceeding other atg8ylation genes, indicating that ATG5 possesses atg8ylation (mATG8s lipid conjugation) independent functions [35,46,53-56]. As recently reported, one such function involves LyHYP contributing to enhanced exocytosis specifically in cells devoid of ATG5 but not of other ATG genes [35]. These developments indicate that ATG5 plays noncanonical roles in autophagy-independent vesicular transport events and homeostasis of the endolysosomal system.

Within the endosomal network, the mammalian retromer complex [57] is one of the several systems regulating vectoral transport of membranes and proteins. These systems include, among others, HOPS, CORVET, retriever, CCC/commander, and retromer [57-64] complexes that often contain and sometimes share VPS subunits. Retromer is a heterotrimer of VPS26A/B, VPS29 and VPS35 subunits [65], first identified in yeast [66]. Retromer sorts an array of endosomal cargo in cooperation with cognate sorting nexins (SNX) [67]. Specifically, this includes SNX-BAR proteins SNX1/2-SNX5/6 [68,69], the mammalian paralogs of yeast Vps5p and Vps17p [66] which can function autonomously as an ESCPE-I complex [70], SNX-PX protein SNX3 [71], and SNX-FERM protein SNX27 containing PX, PDZ and FERM domains [72] and sorting various transporter proteins and signaling receptors including the glucose transporter GLUT1 (SLC2A1) [73]. Retromer, together with adaptors, contributes to the complex protein sorting within the endosomal system [74-76]. Here, using unbiased proteomic approaches

and follow-up mechanistic analyses, we report that retromer complex is among ATG5 interactors. We show that membrane atg8ylation, of which ATG5 is an essential component, affects retromer-dependent cargo sorting. This function is independent of the canonical autophagy pathway or a well-studied form of noncanonical membrane atg8ylation, CASM. Our findings offer a paradigm shift connecting ATG5 and membrane atg8ylation with the retromer system and its function in the endosomal cargo sorting, expanding the scope of atg8ylation machinery and its special component ATG5 beyond the current models.

RESULTS

ATG5 associates with the retromer complex

The unique aspects of Atg5 (Fig. 1A), outside of its role in canonical autophagy, have strong ex vivo and important in vivo phenotypes [52]. Inactivation of Atg5 in myeloid lineage renders mice excessively susceptible to acute infection with *Mycobacterium tuberculosis* attributed to excessive inflammation [35,46,53-56], which did not extend to other phases of infection as tested here in a murine model of latent tuberculosis [77-79] (Fig. S1A-D). In a previous study, we could only partially explain the cellular parameters associated with acute infection, which included degranulation in neutrophils from Atg5$^{fl/fl}$ LysM-Cre^{+} mice [35]. Furthermore, markers of LyHYP (lysosome hypersensitivity phenotype) [35] in ATG5 knockout (KO) cells, such as galectin 3 (Gal3) response, could not be explained by the exocytic phenomena [35]. We thus sought to uncover additional processes (Fig. 1A) affected by ATG5 at the intracellular level. To include factors beyond the known processes, we analyzed proteomic data obtained with APEX2-ATG5 [35] and compared APEX2-ATG5^{WT} with APEX2-ATG5^{K130R} (an ATG5 mutant deficient in conjugation to ATG12) in cells treated with LLOMe, an agent routinely used to cause lysosomal damage [80-85] (Figs. 1B and S2A,B). The proximity biotinylation (APEX2)-based proteomic data indicated the presence in the vicinity of APEX2-ATG5 of several protein complexes that control important membrane trafficking pathways including retromer (Fig. 1B). Beside the retromer VPS subunits, there were very few other VPS proteins (Fig. S2C). VPS proteins were observed in ATG5 proteomic data by others [86] (Fig. S2D). VPS26 and VPS29 showed statistically significant increase in proximity to ATG5 in cells subjected to LLOMe treatment (Fig. S2A-C). Using APEX2-SGALS1 proximity biotinylation LC-MS/MS as a control, we did not observe enrichment of retromer subunits in cells treated with LLOMe (Fig. S2E).

Association of endogenous ATG5 with endogenous retromer subunits (VPS26A, VPS29 and VPS35) was tested in coimmunoprecipitation (co-IP) experiments (Fig. 1C-E). The interaction between retromer and ATG5 was detected in these experiments and showed increased association in cells subjected to lysosomal damage with LLOMe (Fig.

1C-E). Thus, ATG5, a key component of the known atg8ylation E3 ligases [42,87], is found in protein complexes with the retromer and this association is enhanced upon lysosomal damage.

Retromer affects a subset of responses to lysosomal damage

During lysosomal damage a number of processes are set in motion to repair, remove and regenerate/replenish lysosomes [37,80,88-91] including membrane atg8ylation-dependent processes of repair by ESCRT machinery [92] and by lipid transfer via ATG2 [85,93]. We have reported that ATG5 KO cells display elevated Gal3 response to lysosomal damage agents including LLOMe [35]. Gal3 is one of the well-characterized sentinel galectins alerting cellular homeostatic systems to lysosomal damage [37,80,81,88,94]. Based on the observed interactions between ATG5 and retromer, we tested whether retromer, like ATG5 [35], affected Gal3 response to lysosomal damage. We used the previously established quantitative high content microscopy (HCM) approach, which provides unbiased machine-driven image acquisition and data analysis [8,36,80,88,94]. In the experiments herein HCM was based on >500 valid primary objects/cells per well, with a minimum of 5 wells per sample (the independent biological replicates being n≥3) as described [35]. Upon treatment with LLOMe, HeLa$^{VPS35\text{-}KO}$ cells had increased Gal3 puncta relative to HeLa^{WT} cells, comparable to HeLa$^{ATG5\text{-}KO}$ (Fig. 2A,B) [35]. The Gal3 phenotype in VPS35 knockout cells was complemented by expression of GFP-VPS35 (Fig. 2C,D). The observed elevated Gal3 recruitment to damaged lysosomes in the absence of VPS35 cannot be explained by increased pools of LAMP2 organelles in the cells, since the overall complement of lysosomes (quantified by LAMP2 puncta/cell) did not increase in LLOMe treated HeLa cells (Fig. S3A,B). Another marker of lysosomal damage, ubiquitination response [95], was elevated in both VPS35 and ATG5 deficient cells (Figs. 2E,F). This phenotype was confirmed in another cell line, Huh7 (Fig. S3C,D). Thus, VPS35 and ATG5 defects have a similar effect on lysosomes, previously characterized and termed lysosomal hypersensitivity phenotype/LyHYP [35].

Not all aspects of LyHYP, previously observed in ATG5 knockouts [35], were seen in VPS35 KO cells. In the case of ATG5 inactivation, the recruitment of ALIX, an ESCRT component involved in early stages of lysosomal repair [80,96,97] is abrogated [35]. In ATG5 KO cells (Huh7$^{ATG5\text{-}KO}$), recruitment of ALIX to lysosomes was prevented, whereas in VPS35 KO cells (Huh7$^{VPS35\text{-}KO}$ and HeLa$^{VPS35\text{-}KO}$) ALIX was efficiently recruited to lysosomes upon LLOMe treatment (Figs. 2G,H and S3C,D).

The elevated Gal3 and ubiquitin markers of increased lysosomal damage in cells with inactivated VPS35 or ATG5 suggest that both may play a related role in lysosomal resilience to membrane damage, which complements the previously observed effects of aberrant VPS35/retromer on lysosomal morphology and proteolytic capacity [98,99]. The dissimilarities between ATG5 and retromer effects on the ALIX recruitment component can be explained by the previously described perturbed function of the ATG conjugation machinery specifically in ATG5 KO cells affirming the unique additional roles of ATG5 [35]. Nevertheless, the striking similarities between ATG5 KO and VPS35 KO effects on heightened Gal3 and ubiquitin responses to lysosomal membrane damage suggest that the two systems (membrane atg8ylation and retromer) closely intersect.

ATG5 affects retromer function

To avoid the confounding, and possibly indirect, effects of lysosomal damage on endolysosomal sorting and trafficking in cells treated with LLOMe, it was necessary to test the effects of ATG5 KO on retromer function under basal conditions with unperturbed lysosomes. Our co-IP analyses (Fig. 1C-E) indicated that ATG5 can be found in protein complexes with retromer subunits even without the lysosomal damage. We further confirmed this in co-IPs showing that GFP-VPS35 and YFP-VPS29 were found in complexes with endogenous ATG5 in resting cells, whereas an isotype IgG control did not pulldown retromer components (Fig. 3A). Reverse co-IPs with GFP-VPS35 and YFP-VPS29 detected endogenous ATG5 and ATG12-ATG5 complexes in GFP/YFP immunoprecipitates (Fig. 3B).

Having established that ATG5 and retromer interact under basal conditions, we tested the effects of ATG5 KO on localization of a well-established cargo for retromer-dependent sorting, GLUT1 [73,100]. We used Huh7 cells, where we generated a panel of membrane atg8ylation and VPS35 CRISPR knockouts (Fig. S4A), because they have a well-defined localization of GLUT1 at the plasma membrane or as intracellular profiles (Fig. 3C), fully amenable (and comparatively more reliable than in HeLa cells) to unbiased quantification by HCM. ATG5 KO in Huh7 cells resulted in redistribution of GLUT1 from the plasma membrane to intracellular punctate profiles (Figs. 3D and S4B). This phenotype was identical to the one observed in VPS35 KO (Fig. 3D and S4B). The increased intracellular GLUT1 puncta overlapped with the lysosomal marker LAMP2 in both ATG5 KO and VPS35 KO cells (Figs. 3C,E and S4C). A similar albeit morphologically less distinct phenotype was observed in HeLa cells (Figs. S4D-H). GLUT1 is sorted by retromer via VPS26's interactor SNX27, with GLUT1 (and similar cargo) being captured by the PDZ domain of SNX27 [72,73]. In WT cells, SNX27 was found in abundant intracellular profiles (Fig. 3F). In both ATG5 KO and VPS35 KO cells, GLUT1 and SNX27 relocalized to the same intracellular compartment (Fig. 3F,G). We carried out lysosomal purification using the well-established LysoIP method [80,91,94,101], and quantified levels of GLUT1 and SNX27 in lysosomal preparations that were positive for LAMP2 and devoid of GM130 (Golgi) and PDI (ER) (Fig. 3H). Both GLUT1 and SNX27 were enriched in lysosomal preparations from ATG5 KO and VPS35 KO cells relative to the WT cells (Fig. 3H). These experiments biochemically identify the lysosomes as a compartment to which GLUT1 and SNX27 relocalize in ATG5 KO and VSP35 KO cells. The above findings show that a loss of ATG5 affects retromer-controlled trafficking events.

Membrane atg8ylation apparatus contributes to retromer function in GLUT1 sorting

ATG5 is a part of the membrane atg8ylation machinery [25,42,87], also known under the term 'LC3 lipidation' [102], which functions within the canonical autophagy pathway but is

also engaged in a wide array of noncanonical processes [25,38,39,44,103,104]. We tested whether other known components of the atg8ylation apparatus affect retromer. The KOs in Huh7 cells of the components of the prototypical atg8ylation E3 ligase [25,42] included: ATG5 and ATG16L1, as well as the previously characterized Huh7 lines knocked out for E1 and E2 enzymes, ATG7 [35] and ATG3 [37]. These KOs all caused entrapment of GLUT1 in intracellular punctate profiles (Figs. 4A, B) as well as an increase in GLUT1 colocalization with lysosomes ($GLUT1^+$ $LAMP2^+$ profiles; Fig. 4C,D). We tested whether retromer component levels were altered in atg8ylation mutants and found no change in total cellular levels of VPS26, VPS29 and VPS35, tested in ATG3, ATG5 and ATG7 KO Huh7 cells (Fig. S5A,B) as well as in ATG5 KO HeLa cells (Fig. S5C,D).

Furthermore, comparison of the previously characterized $HeLa^{Hexa\text{-}KO}$ cells [105], with all principal mATG8s inactivated, with their isogenic parental $HeLa^{WT}$ cells, showed increased GLUT1 on lysosomes in $HeLa^{Hexa\text{-}KO}$ ($GLUT1^+$ $LAMP2^+$ profiles; Fig. 4E,F). We observed a similar phenotype in separate triple knockouts (TKOs) of LC3 subfamily and GABARAP subfamily of mATG8s [105] compared to $HeLa^{Hexa\text{-}KO}$ (Fig. S5B). Thus, the entire membrane atg8ylation machinery was engaged in and required for proper GLUT-1 sorting.

Canonical autophagy cannot explain effects of membrane atg8ylation on GLUT1 sorting

Membrane atg8ylation and mATGs play roles in diverse processes [25] including canonical autophagy [1]. We tested whether the participation of atg8ylation in canonical autophagy, previously reported to affect retromer-dependent cargo sorting under nutrient-limiting conditions [106,107], is the reason for reduced trafficking of GLUT1 in our experiments. We used KOs in Huh7 cells of ATG13 and FIP200/RB1CC1, two obligatory components of the canonical autophagy initiation machinery [1], to test whether canonical autophagy under the basal conditions used in our study was responsible for the effects on GLUT1 sorting. We found that in the Huh7 cells knocked out for ATG13 [35] or FIP200 [37] there was no increase in intracellular GLUT1 puncta in contrast to the

increase observed with the isogenic ATG5 and VPS35 mutants (Figs. 5A,B). This was mirrored by no increase of GLUT1^{+}LAMP2^{+} profiles in ATG13 and FIP200 KO cells whereas colocalization between GLUT1 and LAMP2A increased in ATG5 and VPS35 mutants (Fig. 5BC). To further confirm that autophagy initiation mutant cells retained the ability to perturb GLUT1 trafficking due to defective atg8ylation, we knocked down ATG5 in FIP200 KO cells (Fig. S5D) and found that GLUT1 puncta and GLUT1^{+}LAMP2^{+} profiles increased even in the FIP200 KO background to an extend nearing in strength the effects of VPS35 knockout (Figs. 5D-F and S5C). Thus, we conclude that atg8ylation but not canonical autophagy affects retromer function under basal conditions and that a functional atg8ylation apparatus is required for proper sorting of the retromer cargo GLUT1.

ATG5 and membrane atg8ylation machinery affect Rab7 localization

Rab7 is considered to be an interactor of the retromer [108]. Rab7 translocates in cells lacking the retromer component VPS35 to lysosomes [109] including endolysosomal domains with lysosomaly positioned mTORC1 regulatory machinery [110]. We thus tested whether absence of ATG5 and components of the atg8ylation apparatus affected Rab7 localization. ATG5, VPS35 as well as knockouts of all major components of the atg8ylation in Huh7 cells, displayed increased Rab7^{+} cytoplasmic profiles (Fig. 6A,B) and overlap between Rab7 and lysosomes (LAMP2) (Figs. 6C and S6A). This was confirmed biochemically using lysosomal purification by LysoIP and immunoblotting for Rab7: there was an increase of Rab7 in lysosomal preparations from ATG5 and VPS35 KO cells (Fig. 6D,E).

This effect extended to other components of the atg8ylation machinery, as KOs in ATG3, ATG7 and ATG16L1 caused a similar effect (Figs. 6A-C and S6A). In contrast, KOs in genes specific for canonical autophagy (ATG13 and FIP200) did not alter intracellular distribution of Rab7 (Figs. 6F-H and S6B). Rab7 distribution was affected by ATG5 knockdown (Fig. S5D) in FIP200 KO cells (Figs. S6B-E). These experiments mirror the effects of ATG5 and atg8ylation on GLUT1 trafficking, showing that ATG5

and atg8ylation machinery but not canonical autophagy is required for proper localization of Rab7.

Agonists of endolysosomal atg8ylation process CASM affect GLUT1 sorting

Membrane atg8ylation has multiple presentations that include not only canonical autophagy but also encompass processes such as CASM [103]. We thus asked whether induction of CASM [93] could affect GLUT1 trafficking. Using LLOMe as one of the inducers of CASM [93], we detect increased membrane atg8ylation (LC3 puncta formation) in response to lysosomal damage (Fig. 7A,B). When cells were treated with LLOMe [93] and another CASM inducer, monensin [29,111,112], GLUT1 trafficking to the plasma membrane was negatively affected and instead GLUT1 accumulated intracellularly and trafficked to lysosomes (Figs. 7C-E and S7A). Thus, lysosomal perturbation and induction of CASM may affect retromer-dependent sorting of GLUT1.

It was previously reported that under glucose starvation conditions, LC3A recruits TBC1D5, a GAP for Rab7 [113-115], away from this small GTPase [106] and a similar phenomenon could be occurring during CASM. However, under CASM-inducing conditions, no change in interactions between TBC1D5 and LC3A were detected (Fig. S7B,C) suggesting that CASM does not affect the status of the TBC1D5-Rab7 system. Moreover, expression of constitutively active $Rab7^{Q67L}$ did not promote trafficking of GLUT1 to plasma membrane but rather caused accumulation of intracellular GLUT1 puncta (Fig. 7F-H).

Membrane atg8ylation and endolysosomal homeostasis affect GLUT1 sorting

A complication of interpreting CASM as a membrane atg8ylation process responsible for effects on retromer-dependent sorting is that CASM is elicited by lysosomal perturbations using lysosomal pH modifying agents [29,103,111,112], and lysosomal stress could be an independent factor preventing proper sorting of GLUT1. Endolysosomal

membrane damage (LLOMe) or perturbations of luminal pH (monensin, bafilomycin A1) negatively affected GLUT1 sorting and caused it to accumulate in lysosomes (Fig. 7C-E). Since bafilomycin A1 does not induce CASM [93] but disturbs luminal pH, we conclude that it is the less acidic luminal pH of the endolysosmal organelles that is sufficient to interfere with the proper sorting of GLUT1.

The above experiments indicate the role of acidification and integrity of endolysosomal compartments in GLUT1 sorting. Membrane atg8ylation is important for lysosomal repair and homeostasis with specific downstream mechanisms. These processes include: (i) ATG2A, which transfers lipids during lysosomal repair [85] and is engaged on damaged lysosomes upon membrane atg8ylation by LC3A [93], and (ii) ESCRT-based lysosomal membrane repair [80,96,97,116], with membrane atg8ylation specifically recruiting an ESCRT regulator ALG2 [92] and ESCRT-I component VPS37A [20]. Hence, we tested whether these established systems, involved in maintenance of lysosomal membrane integrity, represented by ATG2 and VPS37, can explain the mechanism underlying the observed effects of membrane atg8ylation on retromer-dependent trafficking. When U2OS ATG2A/ATG2B double KO cells were compared to parental U2OS WT cells, we observed aberrant GLUT1 trafficking, presented as accumulation of cytoplasmic GLUT1 puncta and increased colocalization of GLUT1 with lysosomes (LAMP2A) (Figs. 8A-C and S8A). A similar effect was observed when the previously characterized VPS37A knockout cells [20] were tested (Figs. 8D-F and S8B). These effects were detected with or without induced lysosomal damage (Fig. 8A-F). We interpret these data as evidence that endolysosomal homeostasis and functionality, which is maintained by membrane atg8ylation at all times even under basal conditions, contributes to proper function of retromer-dependent sorting of its cognate cargo such as GLUT1 (Fig. 8E).

ATG5 effects on retromer function exceed those of membrane atg8ylation

Finally, we addressed the strength of effects on GLUT1 trafficking observed with ATG5 KO vs. KOs in other membrane atg8ylation genes, which were significant in all

experiments but presented effects lower in magnitude than ATG5 KO (Figs. 4 and 6). One possibility was that since ATG3, ATG5, and ATG7 all participate in the same process of membrane atg8ylation, that our KO mutants had unequal gene inactivation levels. This was ruled out by comparing effects of ATG3 KO, ATG5 KO and ATG7 KO cells for their effects on LC3 puncta formation in a well-defined system of starvation-induced autophagy. The results of these analyses indicated that all three KOs had indistinguishable effects on LC3 puncta formation during canonical autophagy induction by starvation (Fig. S8C,D). Thus, the stronger effects of ATG5 KO on retromer vis-à-vis KOs in other atg8ylation genes reflected additional action of ATG5. In the absence of ATG5, less VPS26 and VPS35 could be pulled down in co-IPs with YFP-VPS29 (Fig. S8E-H). We conclude that ATG5, in addition to contributing to the retromer-dependent sorting via membrane atg8ylation and its downstream effector mechanisms which maintain healthy endolysosomal organelles, has additional effects on the retromer.

DISCUSSION

In this study, we have uncovered a new role of ATG5 and membrane atg8ylation machinery beyond the conventional function in canonical autophagy and the hitherto recognized noncanonical processes. ATG5 interacts with the retromer complex, whereas ATG5 and membrane atg8ylation affect retromer function in sorting of its cognate cargo GLUT1. Inactivation of ATG5 and of other membrane atg8ylation genes but not of the genes involved in canonical autophagy perturbs retromer-dependent trafficking. ATG5 and membrane atg8ylation display dual and combined effects on retromer function. The first one is through endolysosomal membrane maintenance ensuring proper cargo sorting by the retromer complex and its adaptor SNX27. The second one is via an association of ATG5 with the retromer complex. These and other activities of ATG5 underly the unique and often perplexing phenotypic manifestations of ATG5 observed in cells and in murine infection models [35,46,51,53-56], which served as the initial impetus for the present study. More generally, the finding that membrane

atg8ylation influences retromer function further expands the range of this process specializing in homeostatic responses to membrane stress, damage and remodeling signals [25,104,117].

Mirroring the role of membrane atg8ylation on retromer function, a loss of VPS35 brings about LyHYP and influences cellular responses to lysosomal damage similarly to the inactivation of ATG5. The parallel between retromer and ATG5 is not perfect, as VPS35 knockout does not divert membrane repair protein ALIX from damaged lysosomes. This can be explained by sequestration of ALIX by the alternative conjugation complex ATG12-ATG3 formed in the absence of ATG5 [35]. The latter phenomenon renders ALIX unavailable for lysosomal repair [35]. VPS35 knockout has no effects on ALIX, and hence the differences between ATG5 and VPS35 in the ALIX component of LyHYP. Nevertheless, inactivation of either ATG5 or VPS35 confers similarly heightened Gal3 [80,81] and ubiquitin [95] responses as hallmarks of elevated lysosomal damage.

A further connectivity between the retromer system and membrane atg8ylation was observed at the level of LC3 puncta formation elicited by noncanonical triggers such as LLOMe treatment, which induces CASM and lysosomal repair. The effects of VPS35 on lysosomal functionality and morphology have been previously noted [98,99], and have been ascribed to the effects of the retromer complex on the recycling of the sorting receptors for lysosomal hydrolases, such as cation-independent mannose 6-phosphate receptor (CI-MPR) [98]. We have detected significant increase in LC3 puncta in VPS35 KO cells stimulated for autophagy by starvation, consistent with the reported diminished lysosomal degradative capacity when VPS35 is absent, an effect ascribed to aberrant CI-MPR sorting [98,99]. Whether CI-MPR is sorted by retromer or independently by the ESCPE-I complex [70] remains controversial [57,70,75,98,110,118-120]. This controversy has been extended to the sorting of cation-dependent mannose 6-phosphate receptor (CD-MPR) [98,121], further confounded by the fact that retriever, which participates in receptor recycling, shares VPS29 subunit with the retromer [61].

In this study, we observed a miss-localization of the small GTPase Rab7 to lysosomes in ATG5 KO cells, paralleling the effects on GLUT1. Retromer and SNX adaptors (SNX3) interact with Rab7 [108]. Rab7 affects retromer-dependent sorting [106,108,109,122]. Depletion of Rab7 reduces endosomal association of retromer [108] whereas retromer status affects Rab7, i.e., in cells with retromer subunits knocked out, Rab7 anomalously accumulates on lysosomes [109]. Consistent with this, we observed that ATG5 KO phenocopied effects of VPS35 KO and caused Rab7 re-localization to lysosomal membranes. Rab7, like other Rabs [114], is controlled by GEFs (Mon1-Cz1), GAPs (ArmusTBC1D2A, TBC1D2B, TBC1D15), and GDI [115]. It is curious that all Rab7 GAPs have LC3 interaction region (LIR) motifs and bind mATG8s: Armus/TBC12DA and TBC1D5 bind LC3A [106,113], GABARAPL1 [113], and LC3C [106]; TBCD12B binds all mATG8s [113,123]; and TBC1D15 binds LC3A [124], LC3B, LC3C, GABARAP, GABARAP L1 and GABARAPL2 [123,124]. Prior elegant studies have shown that genetic ablation of the Rab7 GAP TBC1D5 results in hyperactivation of Rab7 in a wrong intracellular locale (lysosome) [109]. In our work, carried out under basal conditions or in cells subjected to lysosomal damage, we observed both translocation of Rab7 to and entrapment of GLUT1 on lysosomes. However, we did not detect any changes in TBC1D5-mATG8s interactions, suggesting that sequestration of this Rab7 GAP by mATG8s, leading to increased plasma membrane localization of GLUT1 under glucose starvation conditions [106], is not at play here. Furthermore, we found that overexpression of constitutively active Rab7 in cells grown in glucose/nutrient-rich media causes lysosomal retention of GLUT1. This is consistent with the reports by others that perturbances in the retromer-TBC1D5 complex lead to miss-localization of Rab7 to more lysosomal-like subdomains within the endosomal system [110] and that inactivation of Rab7's GAP TBC1D5 leads to entrapment within the endosomal system of the plasma membrane receptors as well as receptors that normally cycle back to the trans-Golgi network [125].

The role of ATG5 in retromer-dependent sorting of GLUT1 appears to have two components, the first one reflects ATG5 being a part of the E3 ligases for membrane atg8ylation and the second one reflects ATG5's being in protein complexes with the core retromer subunits VPS26, VPS29 and VPS35. The latter association potentially

explains the stronger effects of ATG5's absence on GLUT1 sorting relative to the inactivation of other membrane atg8ylation genes. Of note, interactions between ATG5 and retromer are independent of the conjugation status of ATG5, as both ATG12—ATG5 conjugates and unconjugated ATG5 were found in protein immunoprecipitates of retromer components. This is consistent with our LC-MS/MS proteomic data indicating a conjugation status-independent increase in the proximity of ATG5 and retromer subunits during lysosomal damage. One consequence of the association between retromer and ATG5, a key component of the membrane atg8ylation apparatus, is that this could spatially direct proper membrane atg8ylation and be in part responsible for the effects of VPS35 KO on lysosomal quality and sensitivity to membrane stress or injury. In our hands, AlphaFold modeling of ATG5 with retromer components did not yield any high-confidence structures, and the best of the low-to-moderate probability structures when subjected to mutational analysis did not result in disruption of ATG5-retromer association observed by co-IPs (data not shown). Identification of the ATG5 partners that bring it to the vicinity of the retromer is yet to be accomplished and remains one of the limitations of the present study.

We used GLUT1 as a well-defined cargo sorted by the retromer in conjunction with SNX27 [72,73]. SNX27 is a versatile adapter, linking retromer to and controlling endosome-to-plasma membrane recycling of nearly 80 proteins such as signaling receptors, ion channels, amino acid and other nutrient transporters [73]. SNX27 was also missorted in ATG5 deficient cells. This suggests that knockouts in ATG5 and in other membrane atg8ylation genes could have complex pleiotropic effects on cellular functions. Given that ATG5 has a particularly strong impact on retromer-dependent sorting, this could in part explain its unique role in the exquisite susceptibility of Atg5 mutant mice to experimental *M. tuberculosis* infections. Such effects likely contribute to the specific inflammatory action of neutrophils observed in Atg5$^{fl/fl}$ LysM-Cre mice [35,46,53-56]. More narrowly, ATG5 KO-dependent GLUT1 miss-sorting may be one of the contributors to increased *M. tuberculosis* pathogenesis in infection sites. More generally, glucose uptake and metabolism are highly important for normal physiology and in various disease states including immune responses to infection, cancer, neurodegeneration, cardiovascular health, and metabolic disorders. We postulate that

deficiencies or polymorphisms in membrane atg8ylation genes could have contributory roles in health and disease via GLUT1 and additional transporter proteins and signaling receptors that are dependent on retromer for their proper positioning and function in the cell.

In conclusion, we find that the membrane atg8ylation and retromer systems are intertwined, and that they affect each other's biological outputs, one being resilience of lysosomes to basal stress or induced damage and the other being endosomal-plasma membrane protein sorting, both being of fundamental interest and potential therapeutic value.

Acknowledgments

We thank Ryan Peters and Seong Won Choi for carrying out animal infection studies, and Fulvio Reggiori for U2OS ATG2 knockout derivatives. This work was supported by NIH grants R37AI042999 and R01AI111935, and center grant P20GM121176 to V.D. Mass spectrometry analysis, B.P., and M.S., were supported by NIH shared instrumentation grant S10OD021801.

Author contributions

Conceptualization: M.A.P, F.W., E.S.T and V.D.; Formal Analysis: M.A.P., E.S.T., F.W., E.H., Y.H., R.J., B.P., T.L.A.D., and V.D.; Investigation and Validation: M.A.P., E.S.T., F.W., V.D.; Resources: V.D., J.J., M.H.M., Y.H.; Writing – Original Draft: V.D.; Data Curation: M.A.P., F.W., E.S.T., E.H., Y.H., M.S., B.P., and V.D.; Visualization: F.W., E.S.T., E.H., Y.H., V.D.; Supervision: V.D.; Project Administration: V.D.; Funding Acquisition: V.D.

1. Morishita, H., and Mizushima, N. (2019). Diverse Cellular Roles of Autophagy. Annu Rev Cell Dev Biol *35*, 453-475. 10.1146/annurev-cellbio-100818-125300.
2. Cook, A.S.I., and Hurley, J.H. (2023). Toward a standard model for autophagosome biogenesis. J Cell Biol *222*. 10.1083/jcb.202304011.
3. Nguyen, A., Lugarini, F., David, C., Hosnani, P., Alagoz, C., Friedrich, A., Schlutermann, D., Knotkova, B., Patel, A., Parfentev, I., et al. (2023). Metamorphic proteins at the basis of human autophagy initiation and lipid transfer. Mol Cell *83*, 2077-2090 e2012. 10.1016/j.molcel.2023.04.026.
4. Olivas, T.J., Wu, Y., Yu, S., Luan, L., Choi, P., Guinn, E.D., Nag, S., De Camilli, P.V., Gupta, K., and Melia, T.J. (2023). ATG9 vesicles comprise the seed membrane of mammalian autophagosomes. J Cell Biol *222*. 10.1083/jcb.202208088.
5. Kannangara, A.R., Poole, D.M., McEwan, C.M., Youngs, J.C., Weerasekara, V.K., Thornock, A.M., Lazaro, M.T., Balasooriya, E.R., Oh, L.M., Soderblom, E.J., et al. (2021). BioID reveals an ATG9A interaction with ATG13-ATG101 in the degradation of p62/SQSTM1-ubiquitin clusters. EMBO Rep *22*, e51136. 10.15252/embr.202051136.
6. Ren, X., Nguyen, T.N., Lam, W.K., Buffalo, C.Z., Lazarou, M., Yokom, A.L., and Hurley, J.H. (2023). Structural basis for ATG9A recruitment to the ULK1 complex in mitophagy initiation. Sci Adv *9*, eadg2997. 10.1126/sciadv.adg2997.
7. Broadbent, D.G., Barnaba, C., Perez, G.I., and Schmidt, J.C. (2023). Quantitative analysis of autophagy reveals the role of ATG9 and ATG2 in autophagosome formation. J Cell Biol *222*. 10.1083/jcb.202210078.
8. Kumar, S., Javed, R., Mudd, M., Pallikkuth, S., Lidke, K.A., Jain, A., Tangavelou, K., Gudmundsson, S.R., Ye, C., Rusten, T.E., et al. (2021). Mammalian hybrid pre-autophagosomal structure HyPAS generates autophagosomes. Cell *184*, 5950-5969 e5922. 10.1016/j.cell.2021.10.017.
9. Mohan, J., Moparthi, S.B., Girard-Blanc, C., Campisi, D., Blanchard, S., Nugues, C., Rama, S., Salles, A., Penard, E., Vassilopoulos, S., and Wollert, T. (2024). ATG16L1 induces the formation of phagophore-like membrane cups. Nat Struct Mol Biol. 10.1038/s41594-024-01300-y.
10. Axe, E.L., Walker, S.A., Manifava, M., Chandra, P., Roderick, H.L., Habermann, A., Griffiths, G., and Ktistakis, N.T. (2008). Autophagosome formation from membrane compartments enriched in phosphatidylinositol 3-phosphate and dynamically connected to the endoplasmic reticulum. J Cell Biol *182*, 685-701.
11. Nahse, V., Raiborg, C., Tan, K.W., Mork, S., Torgersen, M.L., Wenzel, E.M., Nager, M., Salo, V.T., Johansen, T., Ikonen, E., et al. (2023). ATPase activity of DFCP1 controls selective autophagy. Nat Commun *14*, 4051. 10.1038/s41467-023-39641-9.
12. Valverde, D.P., Yu, S., Boggavarapu, V., Kumar, N., Lees, J.A., Walz, T., Reinisch, K.M., and Melia, T.J. (2019). ATG2 transports lipids to promote autophagosome biogenesis. J Cell Biol *218*, 1787-1798. 10.1083/jcb.201811139.

534 13. Maeda, S., Otomo, C., and Otomo, T. (2019). The autophagic membrane tether ATG2A
535 transfers lipids between membranes. Elife *8*. 10.7554/eLife.45777.
536 14. Dabrowski, R., Tulli, S., and Graef, M. (2023). Parallel phospholipid transfer by Vps13 and
537 Atg2 determines autophagosome biogenesis dynamics. J Cell Biol *222*.
538 10.1083/jcb.202211039.
539 15. Turco, E., Witt, M., Abert, C., Bock-Bierbaum, T., Su, M.Y., Trapannone, R., Sztacho, M.,
540 Danieli, A., Shi, X., Zaffagnini, G., et al. (2019). FIP200 Claw Domain Binding to p62
541 Promotes Autophagosome Formation at Ubiquitin Condensates. Mol Cell *74*, 330-346
542 e311. 10.1016/j.molcel.2019.01.035.
543 16. Lamark, T., and Johansen, T. (2021). Mechanisms of Selective Autophagy. Annu Rev Cell
544 Dev Biol *37*, 143-169. 10.1146/annurev-cellbio-120219-035530.
545 17. Flower, T.G., Takahashi, Y., Hudait, A., Rose, K., Tjahjono, N., Pak, A.J., Yokom, A.L.,
546 Liang, X., Wang, H.G., Bouamr, F., et al. (2020). A helical assembly of human ESCRT-I
547 scaffolds reverse-topology membrane scission. Nat Struct Mol Biol *27*, 570-580.
548 10.1038/s41594-020-0426-4.
549 18. Takahashi, Y., Liang, X., Hattori, T., Tang, Z., He, H., Chen, H., Liu, X., Abraham, T.,
550 Imamura-Kawasawa, Y., Buchkovich, N.J., et al. (2019). VPS37A directs ESCRT
551 recruitment for phagophore closure. J Cell Biol *218*, 3336-3354. 10.1083/jcb.201902170.
552 19. Takahashi, Y., He, H., Tang, Z., Hattori, T., Liu, Y., Young, M.M., Serfass, J.M., Chen, L.,
553 Gebru, M., Chen, C., et al. (2018). An autophagy assay reveals the ESCRT-III component
554 CHMP2A as a regulator of phagophore closure. Nat Commun *9*, 2855. 10.1038/s41467-
555 018-05254-w.
556 20. Javed, R., Jain, A., Duque, T., Hendrix, E., Paddar, M.A., Khan, S., Claude-Taupin, A., Jia,
557 J., Allers, L., Wang, F., et al. (2023). Mammalian ATG8 proteins maintain
558 autophagosomal membrane integrity through ESCRTs. EMBO J, e112845.
559 10.15252/embj.2022112845.
560 21. Zhao, Y.G., and Zhang, H. (2019). Autophagosome maturation: An epic journey from the
561 ER to lysosomes. J Cell Biol *218*, 757-770. 10.1083/jcb.201810099.
562 22. Ponpuak, M., Mandell, M.A., Kimura, T., Chauhan, S., Cleyrat, C., and Deretic, V. (2015).
563 Secretory autophagy. Curr Opin Cell Biol *35*, 106-116. 10.1016/j.ceb.2015.04.016.
564 23. Yamamoto, H., Zhang, S., and Mizushima, N. (2023). Autophagy genes in biology and
565 disease. Nat Rev Genet *24*, 382-400. 10.1038/s41576-022-00562-w.
566 24. Galluzzi, L., and Green, D.R. (2019). Autophagy-Independent Functions of the Autophagy
567 Machinery. Cell *177*, 1682-1699. 10.1016/j.cell.2019.05.026.
568 25. Deretic, V., and Lazarou, M. (2022). A guide to membrane atg8ylation and autophagy
569 with reflections on immunity. J Cell Biol *221*. 10.1083/jcb.202203083.
570 26. Sanjuan, M.A., Dillon, C.P., Tait, S.W., Moshiach, S., Dorsey, F., Connell, S., Komatsu, M.,
571 Tanaka, K., Cleveland, J.L., Withoff, S., and Green, D.R. (2007). Toll-like receptor
572 signalling in macrophages links the autophagy pathway to phagocytosis. Nature *450*,
573 1253-1257.
574 27. Heckmann, B.L., Teubner, B.J.W., Tummers, B., Boada-Romero, E., Harris, L., Yang, M.,
575 Guy, C.S., Zakharenko, S.S., and Green, D.R. (2019). LC3-Associated Endocytosis
576 Facilitates beta-Amyloid Clearance and Mitigates Neurodegeneration in Murine
577 Alzheimer's Disease. Cell *178*, 536-551 e514. 10.1016/j.cell.2019.05.056.

578 28. Sonder, S.L., Hager, S.C., Heitmann, A.S.B., Frankel, L.B., Dias, C., Simonsen, A.C., and
579 Nylandsted, J. (2021). Restructuring of the plasma membrane upon damage by LC3-
580 associated macropinocytosis. Sci Adv *7*. 10.1126/sciadv.abg1969.
581 29. Goodwin, J.M., Walkup, W.G.t., Hooper, K., Li, T., Kishi-Itakura, C., Ng, A., Lehmberg, T.,
582 Jha, A., Kommineni, S., Fletcher, K., et al. (2021). GABARAP sequesters the FLCN-FNIP
583 tumor suppressor complex to couple autophagy with lysosomal biogenesis. Sci Adv *7*,
584 eabj2485. 10.1126/sciadv.abj2485.
585 30. Hooper, K.M., Jacquin, E., Li, T., Goodwin, J.M., Brumell, J.H., Durgan, J., and Florey, O.
586 (2022). V-ATPase is a universal regulator of LC3-associated phagocytosis and non-
587 canonical autophagy. J Cell Biol *221*. 10.1083/jcb.202105112.
588 31. Xu, Y., Zhou, P., Cheng, S., Lu, Q., Nowak, K., Hopp, A.K., Li, L., Shi, X., Zhou, Z., Gao, W.,
589 et al. (2019). A Bacterial Effector Reveals the V-ATPase-ATG16L1 Axis that Initiates
590 Xenophagy. Cell *178*, 552-566 e520. 10.1016/j.cell.2019.06.007.
591 32. Fischer, T.D., Wang, C., Padman, B.S., Lazarou, M., and Youle, R.J. (2020). STING induces
592 LC3B lipidation onto single-membrane vesicles via the V-ATPase and ATG16L1-WD40
593 domain. J Cell Biol *219*. 10.1083/jcb.202009128.
594 33. Xu, Y., Cheng, S., Zeng, H., Zhou, P., Ma, Y., Li, L., Liu, X., Shao, F., and Ding, J. (2022). ARF
595 GTPases activate Salmonella effector SopF to ADP-ribosylate host V-ATPase and inhibit
596 endomembrane damage-induced autophagy. Nat Struct Mol Biol *29*, 67-77.
597 10.1038/s41594-021-00710-6.
598 34. Sun, Y., Wang, X., Yang, X., Wang, L., Ding, J., Wang, C.C., Zhang, H., and Wang, X. (2023).
599 V-ATPase recruitment to ER exit sites switches COPII-mediated transport to lysosomal
600 degradation. Dev Cell *58*, 2761-2775 e2765. 10.1016/j.devcel.2023.10.007.
601 35. Wang, F., Peters, R., Jia, J., Mudd, M., Salemi, M., Allers, L., Javed, R., Duque, T.L.A.,
602 Paddar, M.A., Trosdal, E.S., et al. (2023). ATG5 provides host protection acting as a
603 switch in the atg8ylation cascade between autophagy and secretion. Dev Cell *58*, 866-
604 884 e868. 10.1016/j.devcel.2023.03.014.
605 36. Claude-Taupin, A., Jia, J., Bhujabal, Z., Garfa-Traore, M., Kumar, S., da Silva, G.P.D.,
606 Javed, R., Gu, Y., Allers, L., Peters, R., et al. (2021). ATG9A protects the plasma
607 membrane from programmed and incidental permeabilization. Nat Cell Biol *23*, 846-
608 858. 10.1038/s41556-021-00706-w.
609 37. Jia, J., Wang, F., Bhujabal, Z., Peters, R., Mudd, M., Duque, T., Allers, L., Javed, R., Salemi,
610 M., Behrends, C., et al. (2022). Stress granules and mTOR are regulated by membrane
611 atg8ylation during lysosomal damage. J Cell Biol *221*. 10.1083/jcb.202207091.
612 38. Kaur, N., de la Ballina, L.R., Haukaas, H.S., Torgersen, M.L., Radulovic, M., Munson, M.J.,
613 Sabirsh, A., Stenmark, H., Simonsen, A., Carlsson, S.R., and Lystad, A.H. (2023). TECPR1 is
614 activated by damage-induced sphingomyelin exposure to mediate noncanonical
615 autophagy. EMBO J, e113105. 10.15252/embj.2022113105.
616 39. Corkery, D.P., Castro-Gonzalez, S., Knyazeva, A., Herzog, L.K., and Wu, Y.W. (2023). An
617 ATG12-ATG5-TECPR1 E3-like complex regulates unconventional LC3 lipidation at
618 damaged lysosomes. EMBO Rep, e56841. 10.15252/embr.202356841.
619 40. Solvik, T.A., Nguyen, T.A., Tony Lin, Y.H., Marsh, T., Huang, E.J., Wiita, A.P., Debnath, J.,
620 and Leidal, A.M. (2022). Secretory autophagy maintains proteostasis upon lysosome
621 inhibition. J Cell Biol *221*. 10.1083/jcb.202110151.

622 41. Leidal, A.M., Huang, H.H., Marsh, T., Solvik, T., Zhang, D., Ye, J., Kai, F., Goldsmith, J., Liu,
623 J.Y., Huang, Y.H., et al. (2020). The LC3-conjugation machinery specifies the loading of
624 RNA-binding proteins into extracellular vesicles. Nat Cell Biol *22*, 187-199.
625 10.1038/s41556-019-0450-y.
626 42. Mizushima, N. (2020). The ATG conjugation systems in autophagy. Curr Opin Cell Biol *63*,
627 1-10. 10.1016/j.ceb.2019.12.001.
628 43. Rao, S., Skulsuppaisarn, M., Strong, L.M., Ren, X., Lazarou, M., Hurley, J.H., and Hummer,
629 G. (2024). Three-step docking by WIPI2, ATG16L1, and ATG3 delivers LC3 to the
630 phagophore. Sci Adv *10*, eadj8027. 10.1126/sciadv.adj8027.
631 44. Boyle, K.B., Ellison, C.J., Elliott, P.R., Schuschnig, M., Grimes, K., Dionne, M.S., Sasakawa,
632 C., Munro, S., Martens, S., and Randow, F. (2023). TECPR1 conjugates LC3 to damaged
633 endomembranes upon detection of sphingomyelin exposure. EMBO J, e113012.
634 10.15252/embj.2022113012.
635 45. Radoshevich, L., Murrow, L., Chen, N., Fernandez, E., Roy, S., Fung, C., and Debnath, J.
636 (2010). ATG12 conjugation to ATG3 regulates mitochondrial homeostasis and cell death.
637 Cell *142*, 590-600. S0092-8674(10)00787-7 [pii]
638 10.1016/j.cell.2010.07.018.
639 46. Castillo, E.F., Dekonenko, A., Arko-Mensah, J., Mandell, M.A., Dupont, N., Jiang, S.,
640 Delgado-Vargas, M., Timmins, G.S., Bhattacharya, D., Yang, H., et al. (2012). Autophagy
641 protects against active tuberculosis by suppressing bacterial burden and inflammation. P
642 Natl Acad Sci USA *109*, E3168-3176. 10.1073/pnas.1210500109.
643 47. Hwang, S., Maloney, N.S., Bruinsma, M.W., Goel, G., Duan, E., Zhang, L., Shrestha, B.,
644 Diamond, M.S., Dani, A., Sosnovtsev, S.V., et al. (2012). Nondegradative role of Atg5-
645 Atg12/ Atg16L1 autophagy protein complex in antiviral activity of interferon gamma.
646 Cell Host Microbe *11*, 397-409. 10.1016/j.chom.2012.03.002.
647 48. Gu, Y., Princely Abudu, Y., Kumar, S., Bissa, B., Choi, S.W., Jia, J., Lazarou, M., Eskelinen,
648 E.L., Johansen, T., and Deretic, V. (2019). Mammalian Atg8 proteins regulate lysosome
649 and autolysosome biogenesis through SNAREs. EMBO J *38*, e101994.
650 10.15252/embj.2019101994.
651 49. Eren, E., Planes, R., Bagayoko, S., Bordignon, P.J., Chaoui, K., Hessel, A., Santoni, K.,
652 Pinilla, M., Lagrange, B., Burlet-Schiltz, O., et al. (2020). Irgm2 and Gate-16 cooperatively
653 dampen Gram-negative bacteria-induced caspase-11 response. EMBO Rep *21*, e50829.
654 10.15252/embr.202050829.
655 50. Wang, Y.T., Zaitsev, K., Lu, Q., Li, S., Schaiff, W.T., Kim, K.W., Droit, L., Wilen, C.B., Desai,
656 C., Balce, D.R., et al. (2020). Select autophagy genes maintain quiescence of tissue-
657 resident macrophages and increase susceptibility to Listeria monocytogenes. Nat
658 Microbiol *5*, 272-281. 10.1038/s41564-019-0633-0.
659 51. Virgin, H.W., and Levine, B. (2009). Autophagy genes in immunity. Nat Immunol *10*, 461-
660 470.
661 52. Deretic, V., and Wang, F. (2023). Autophagy is part of the answer to tuberculosis. Nat
662 Microbiol *8*, 762-763. 10.1038/s41564-023-01373-3.
663 53. Watson, R.O., Manzanillo, P.S., and Cox, J.S. (2012). Extracellular M. tuberculosis DNA
664 Targets Bacteria for Autophagy by Activating the Host DNA-Sensing Pathway. Cell *150*,
665 803-815. 10.1016/j.cell.2012.06.040.

666 54. Kimmey, J.M., Huynh, J.P., Weiss, L.A., Park, S., Kambal, A., Debnath, J., Virgin, H.W., and
667 Stallings, C.L. (2015). Unique role for ATG5 in neutrophil-mediated immunopathology
668 during M. tuberculosis infection. Nature *528*, 565-569. 10.1038/nature16451.
669 55. Golovkine, G.R., Roberts, A.W., Morrison, H.M., Rivera-Lugo, R., McCall, R.M., Nilsson,
670 H., Garelis, N.E., Repasy, T., Cronce, M., Budzik, J., et al. (2023). Autophagy restricts
671 Mycobacterium tuberculosis during acute infection in mice. Nat Microbiol *8*, 819-832.
672 10.1038/s41564-023-01354-6.
673 56. Kinsella, R.L., Kimmey, J.M., Smirnov, A., Woodson, R., Gaggioli, M.R., Chavez, S.M.,
674 Kreamalmeyer, D., and Stallings, C.L. (2023). Autophagy prevents early proinflammatory
675 responses and neutrophil recruitment during Mycobacterium tuberculosis infection
676 without affecting pathogen burden in macrophages. PLoS Biol *21*, e3002159.
677 10.1371/journal.pbio.3002159.
678 57. Seaman, M.N.J. (2021). The Retromer Complex: From Genesis to Revelations. Trends
679 Biochem Sci *46*, 608-620. 10.1016/j.tibs.2020.12.009.
680 58. Burstein, E., Hoberg, J.E., Wilkinson, A.S., Rumble, J.M., Csomos, R.A., Komarck, C.M.,
681 Maine, G.N., Wilkinson, J.C., Mayo, M.W., and Duckett, C.S. (2005). COMMD proteins, a
682 novel family of structural and functional homologs of MURR1. J Biol Chem *280*, 22222-
683 22232. 10.1074/jbc.M501928200.
684 59. Bonifacino, J.S., and Hurley, J.H. (2008). Retromer. Curr Opin Cell Biol *20*, 427-436.
685 10.1016/j.ceb.2008.03.009.
686 60. Balderhaar, H.J., and Ungermann, C. (2013). CORVET and HOPS tethering complexes -
687 coordinators of endosome and lysosome fusion. J Cell Sci *126*, 1307-1316.
688 10.1242/jcs.107805.
689 61. McNally, K.E., Faulkner, R., Steinberg, F., Gallon, M., Ghai, R., Pim, D., Langton, P.,
690 Pearson, N., Danson, C.M., Nagele, H., et al. (2017). Retriever is a multiprotein complex
691 for retromer-independent endosomal cargo recycling. Nat Cell Biol *19*, 1214-1225.
692 10.1038/ncb3610.
693 62. Mallam, A.L., and Marcotte, E.M. (2017). Systems-wide Studies Uncover Commander, a
694 Multiprotein Complex Essential to Human Development. Cell Syst *4*, 483-494.
695 10.1016/j.cels.2017.04.006.
696 63. Shvarev, D., Schoppe, J., Konig, C., Perz, A., Fullbrunn, N., Kiontke, S., Langemeyer, L.,
697 Januliene, D., Schnelle, K., Kummel, D., et al. (2022). Structure of the HOPS tethering
698 complex, a lysosomal membrane fusion machinery. Elife *11*. 10.7554/eLife.80901.
699 64. Healy, M.D., McNally, K.E., Butkovic, R., Chilton, M., Kato, K., Sacharz, J., McConville, C.,
700 Moody, E.R.R., Shaw, S., Planelles-Herrero, V.J., et al. (2023). Structure of the endosomal
701 Commander complex linked to Ritscher-Schinzel syndrome. Cell *186*, 2219-2237 e2229.
702 10.1016/j.cell.2023.04.003.
703 65. Haft, C.R., de la Luz Sierra, M., Bafford, R., Lesniak, M.A., Barr, V.A., and Taylor, S.I.
704 (2000). Human orthologs of yeast vacuolar protein sorting proteins Vps26, 29, and 35:
705 assembly into multimeric complexes. Mol Biol Cell *11*, 4105-4116.
706 10.1091/mbc.11.12.4105.
707 66. Seaman, M.N., McCaffery, J.M., and Emr, S.D. (1998). A membrane coat complex
708 essential for endosome-to-Golgi retrograde transport in yeast. J Cell Biol *142*, 665-681.
709 10.1083/jcb.142.3.665.

710 67. Gallon, M., and Cullen, P.J. (2015). Retromer and sorting nexins in endosomal sorting.
711 Biochem Soc Trans *43*, 33-47. 10.1042/BST20140290.
712 68. Rojas, R., van Vlijmen, T., Mardones, G.A., Prabhu, Y., Rojas, A.L., Mohammed, S., Heck,
713 A.J., Raposo, G., van der Sluijs, P., and Bonifacino, J.S. (2008). Regulation of retromer
714 recruitment to endosomes by sequential action of Rab5 and Rab7. J Cell Biol *183*, 513-
715 526. 10.1083/jcb.200804048.
716 69. Wassmer, T., Attar, N., Bujny, M.V., Oakley, J., Traer, C.J., and Cullen, P.J. (2007). A loss-
717 of-function screen reveals SNX5 and SNX6 as potential components of the mammalian
718 retromer. J Cell Sci *120*, 45-54. 10.1242/jcs.03302.
719 70. Simonetti, B., Paul, B., Chaudhari, K., Weeratunga, S., Steinberg, F., Gorla, M., Heesom,
720 K.J., Bashaw, G.J., Collins, B.M., and Cullen, P.J. (2019). Molecular identification of a BAR
721 domain-containing coat complex for endosomal recycling of transmembrane proteins.
722 Nature Cell Biology *21*, 1219-1233. 10.1038/s41556-019-0393-3.
723 71. Harterink, M., Port, F., Lorenowicz, M.J., McGough, I.J., Silhankova, M., Betist, M.C., van
724 Weering, J.R.T., van Heesbeen, R., Middelkoop, T.C., Basler, K., et al. (2011). A SNX3-
725 dependent retromer pathway mediates retrograde transport of the Wnt sorting
726 receptor Wntless and is required for Wnt secretion. Nat Cell Biol *13*, 914-923.
727 10.1038/ncb2281.
728 72. Gallon, M., Clairfeuille, T., Steinberg, F., Mas, C., Ghai, R., Sessions, R.B., Teasdale, R.D.,
729 Collins, B.M., and Cullen, P.J. (2014). A unique PDZ domain and arrestin-like fold
730 interaction reveals mechanistic details of endocytic recycling by SNX27-retromer. Proc
731 Natl Acad Sci U S A *111*, E3604-3613. 10.1073/pnas.1410552111.
732 73. Steinberg, F., Gallon, M., Winfield, M., Thomas, E.C., Bell, A.J., Heesom, K.J., Tavaré,
733 J.M., and Cullen, P.J. (2013). A global analysis of SNX27-retromer assembly and cargo
734 specificity reveals a function in glucose and metal ion transport. Nat Cell Biol *15*, 461-
735 471. 10.1038/ncb2721.
736 74. Tu, Y., and Seaman, M.N.J. (2021). Navigating the Controversies of Retromer-Mediated
737 Endosomal Protein Sorting. Front Cell Dev Biol *9*, 658741. 10.3389/fcell.2021.658741.
738 75. Buser, D.P., and Spang, A. (2023). Protein sorting from endosomes to the TGN. Front Cell
739 Dev Biol *11*, 1140605. 10.3389/fcell.2023.1140605.
740 76. Carosi, J.M., Denton, D., Kumar, S., and Sargeant, T.J. (2023). Receptor Recycling by
741 Retromer. Mol Cell Biol *43*, 317-334. 10.1080/10985549.2023.2222053.
742 77. McCune, R.M., Jr., and Tompsett, R. (1956). Fate of Mycobacterium tuberculosis in
743 mouse tissues as determined by the microbial enumeration technique. I. The
744 persistence of drug-susceptible tubercle bacilli in the tissues despite prolonged
745 antimicrobial therapy. J Exp Med *104*, 737-762.
746 78. McCune, R.M., Jr., McDermott, W., and Tompsett, R. (1956). The fate of Mycobacterium
747 tuberculosis in mouse tissues as determined by the microbial enumeration technique. II.
748 The conversion of tuberculous infection to the latent state by the administration of
749 pyrazinamide and a companion drug. J Exp Med *104*, 763-802.
750 79. Scanga, C.A., Mohan, V.P., Joseph, H., Yu, K., Chan, J., and Flynn, J.L. (1999). Reactivation
751 of latent tuberculosis: variations on the Cornell murine model. Infect Immun *67*, 4531-
752 4538.

753 80. Jia, J., Claude-Taupin, A., Gu, Y., Choi, S.W., Peters, R., Bissa, B., Mudd, M.H., Allers, L.,
754 Pallikkuth, S., Lidke, K.A., et al. (2020). Galectin-3 Coordinates a Cellular System for
755 Lysosomal Repair and Removal. Dev Cell *52*, 69-87 e68. 10.1016/j.devcel.2019.10.025.
756 81. Aits, S., Kricker, J., Liu, B., Ellegaard, A.M., Hamalisto, S., Tvingsholm, S., Corcelle-
757 Termeau, E., Hogh, S., Farkas, T., Holm Jonassen, A., et al. (2015). Sensitive detection of
758 lysosomal membrane permeabilization by lysosomal galectin puncta assay. Autophagy
759 *11*, 1408-1424. 10.1080/15548627.2015.1063871.
760 82. Thiele, D.L., and Lipsky, P.E. (1990). Mechanism of L-leucyl-L-leucine methyl ester-
761 mediated killing of cytotoxic lymphocytes: dependence on a lysosomal thiol protease,
762 dipeptidyl peptidase I, that is enriched in these cells. Proc Natl Acad Sci U S A *87*, 83-87.
763 83. Eriksson, I., Waster, P., and Ollinger, K. (2020). Restoration of lysosomal function after
764 damage is accompanied by recycling of lysosomal membrane proteins. Cell Death Dis *11*,
765 370. 10.1038/s41419-020-2527-8.
766 84. Bonet-Ponce, L., Beilina, A., Williamson, C.D., Lindberg, E., Kluss, J.H., Saez-Atienzar, S.,
767 Landeck, N., Kumaran, R., Mamais, A., Bleck, C.K.E., et al. (2020). LRRK2 mediates
768 tubulation and vesicle sorting from lysosomes. Sci Adv *6*. 10.1126/sciadv.abb2454.
769 85. Tan, J.X., and Finkel, T. (2022). A phosphoinositide signalling pathway mediates rapid
770 lysosomal repair. Nature *609*, 815-821. 10.1038/s41586-022-05164-4.
771 86. Baines, K., Yoshioka, K., Takuwa, Y., and Lane, J.D. (2022). The ATG5 interactome links
772 clathrin-mediated vesicular trafficking with the autophagosome assembly machinery.
773 Autophagy Rep *1*, 88-118. 10.1080/27694127.2022.2042054.
774 87. Deretic, V., and Klionsky, D.J. (2024). An expanding repertoire of E3 ligases in membrane
775 Atg8ylation. Nat Cell Biol *26*, 307-308. 10.1038/s41556-023-01329-z.
776 88. Jia, J., Abudu, Y.P., Claude-Taupin, A., Gu, Y., Kumar, S., Choi, S.W., Peters, R., Mudd,
777 M.H., Allers, L., Salemi, M., et al. (2018). Galectins Control mTOR in Response to
778 Endomembrane Damage. Mol Cell *70*, 120-135 e128. 10.1016/j.molcel.2018.03.009.
779 89. Nakamura, S., Shigeyama, S., Minami, S., Shima, T., Akayama, S., Matsuda, T., Esposito,
780 A., Napolitano, G., Kuma, A., Namba-Hamano, T., et al. (2020). LC3 lipidation is essential
781 for TFEB activation during the lysosomal damage response to kidney injury. Nat Cell Biol
782 *22*, 1252-1263. 10.1038/s41556-020-00583-9.
783 90. Jia, J., Abudu, Y.P., Claude-Taupin, A., Gu, Y., Kumar, S., Choi, S.W., Peters, R., Mudd,
784 M.H., Allers, L., Salemi, M., et al. (2019). Galectins control MTOR and AMPK in response
785 to lysosomal damage to induce autophagy. Autophagy *15*, 169-171.
786 10.1080/15548627.2018.1505155.
787 91. Eapen, V.V., Swarup, S., Hoyer, M.J., Paulo, J.A., and Harper, J.W. (2021). Quantitative
788 proteomics reveals the selectivity of ubiquitin-binding autophagy receptors in the
789 turnover of damaged lysosomes by lysophagy. Elife *10*. 10.7554/eLife.72328.
790 92. Corkery, D.P., Li, S., Wijayatunga, D., Herzog, L.K., Knyazeva, A., and Wu, Y.-W. (2024).
791 ESCRT recruitment to damaged lysosomes is dependent on the ATG8 E3-like ligases.
792 bioRxiv, 2024.2004.2030.591897. 10.1101/2024.04.30.591897.
793 93. Cross, J., Durgan, J., McEwan, D.G., Tayler, M., Ryan, K.M., and Florey, O. (2023).
794 Lysosome damage triggers direct ATG8 conjugation and ATG2 engagement via non-
795 canonical autophagy. J Cell Biol *222*. 10.1083/jcb.202303078.

796 94. Jia, J., Bissa, B., Brecht, L., Allers, L., Choi, S.W., Gu, Y., Zbinden, M., Burge, M.R.,
797 Timmins, G., Hallows, K., et al. (2020). AMPK, a Regulator of Metabolism and Autophagy,
798 Is Activated by Lysosomal Damage via a Novel Galectin-Directed Ubiquitin Signal
799 Transduction System. Mol Cell. 10.1016/j.molcel.2019.12.028.
800 95. Papadopoulos, C., Kirchner, P., Bug, M., Grum, D., Koerver, L., Schulze, N., Poehler, R.,
801 Dressler, A., Fengler, S., Arhzaouy, K., et al. (2017). VCP/p97 cooperates with YOD1,
802 UBXD1 and PLAA to drive clearance of ruptured lysosomes by autophagy. EMBO J *36*,
803 135-150. 10.15252/embj.201695148.
804 96. Skowyra, M.L., Schlesinger, P.H., Naismith, T.V., and Hanson, P.I. (2018). Triggered
805 recruitment of ESCRT machinery promotes endolysosomal repair. Science *360*.
806 10.1126/science.aar5078.
807 97. Radulovic, M., Schink, K.O., Wenzel, E.M., Nahse, V., Bongiovanni, A., Lafont, F., and
808 Stenmark, H. (2018). ESCRT-mediated lysosome repair precedes lysophagy and
809 promotes cell survival. EMBO J *37*. 10.15252/embj.201899753.
810 98. Cui, Y., Carosi, J.M., Yang, Z., Ariotti, N., Kerr, M.C., Parton, R.G., Sargeant, T.J., and
811 Teasdale, R.D. (2019). Retromer has a selective function in cargo sorting via endosome
812 transport carriers. J Cell Biol *218*, 615-631. 10.1083/jcb.201806153.
813 99. Daly, J.L., Danson, C.M., Lewis, P.A., Zhao, L., Riccardo, S., Di Filippo, L., Cacchiarelli, D.,
814 Lee, D., Cross, S.J., Heesom, K.J., et al. (2023). Multi-omic approach characterises the
815 neuroprotective role of retromer in regulating lysosomal health. Nat Commun *14*, 3086.
816 10.1038/s41467-023-38719-8.
817 100. McGough, I.J., Steinberg, F., Gallon, M., Yatsu, A., Ohbayashi, N., Heesom, K.J., Fukuda,
818 M., and Cullen, P.J. (2014). Identification of molecular heterogeneity in SNX27-retromer-
819 mediated endosome-to-plasma-membrane recycling. J Cell Sci *127*, 4940-4953.
820 10.1242/jcs.156299.
821 101. Wyant, G.A., Abu-Remaileh, M., Frenkel, E.M., Laqtom, N.N., Dharamdasani, V., Lewis,
822 C.A., Chan, S.H., Heinze, I., Ori, A., and Sabatini, D.M. (2018). NUFIP1 is a ribosome
823 receptor for starvation-induced ribophagy. Science *360*, 751-758.
824 10.1126/science.aar2663.
825 102. Kabeya, Y., Mizushima, N., Ueno, T., Yamamoto, A., Kirisako, T., Noda, T., Kominami, E.,
826 Ohsumi, Y., and Yoshimori, T. (2000). LC3, a mammalian homologue of yeast Apg8p, is
827 localized in autophagosome membranes after processing. Embo J *19*, 5720-5728.
828 103. Durgan, J., and Florey, O. (2022). Many roads lead to CASM: Diverse stimuli of
829 noncanonical autophagy share a unifying molecular mechanism. Sci Adv *8*, eabo1274.
830 10.1126/sciadv.abo1274.
831 104. Deretic, V., Duque, T., Trosdal, E., Paddar, M., Javed, R., and Akepati, P. (2024).
832 Membrane atg8ylation in Canonical and Noncanonical Autophagy. J Mol Biol, 168532.
833 10.1016/j.jmb.2024.168532.
834 105. Nguyen, T.N., Padman, B.S., Usher, J., Oorschot, V., Ramm, G., and Lazarou, M. (2016).
835 Atg8 family LC3/GABARAP proteins are crucial for autophagosome-lysosome fusion but
836 not autophagosome formation during PINK1/Parkin mitophagy and starvation. J Cell Biol
837 *215*, 857-874. 10.1083/jcb.201607039.

838 106. Roy, S., Leidal, A.M., Ye, J., Ronen, S.M., and Debnath, J. (2017). Autophagy-Dependent
839 Shuttling of TBC1D5 Controls Plasma Membrane Translocation of GLUT1 and Glucose
840 Uptake. Mol Cell *67*, 84-95 e85. 10.1016/j.molcel.2017.05.020.
841 107. Carosi, J.M., Hein, L.K., Sandow, J.J., Dang, L.V.P., Hattersley, K., Denton, D., Kumar, S.,
842 and Sargeant, T.J. (2024). Autophagy captures the retromer-TBC1D5 complex to inhibit
843 receptor recycling. Autophagy *20*, 863-882. 10.1080/15548627.2023.2281126.
844 108. Harrison, M.S., Hung, C.S., Liu, T.T., Christiano, R., Walther, T.C., and Burd, C.G. (2014). A
845 mechanism for retromer endosomal coat complex assembly with cargo. Proc Natl Acad
846 Sci U S A *111*, 267-272. 10.1073/pnas.1316482111.
847 109. Jimenez-Orgaz, A., Kvainickas, A., Nagele, H., Denner, J., Eimer, S., Dengjel, J., and
848 Steinberg, F. (2018). Control of RAB7 activity and localization through the retromer-
849 TBC1D5 complex enables RAB7-dependent mitophagy. EMBO J *37*, 235-254.
850 10.15252/embj.201797128.
851 110. Kvainickas, A., Nagele, H., Qi, W., Dokladal, L., Jimenez-Orgaz, A., Stehl, L., Gangurde, D.,
852 Zhao, Q., Hu, Z., Dengjel, J., et al. (2019). Retromer and TBC1D5 maintain late
853 endosomal RAB7 domains to enable amino acid-induced mTORC1 signaling. J Cell Biol
854 *218*, 3019-3038. 10.1083/jcb.201812110.
855 111. Florey, O., Gammoh, N., Kim, S.E., Jiang, X., and Overholtzer, M. (2015). V-ATPase and
856 osmotic imbalances activate endolysosomal LC3 lipidation. Autophagy *11*, 88-99.
857 10.4161/15548627.2014.984277.
858 112. Fletcher, K., Ulferts, R., Jacquin, E., Veith, T., Gammoh, N., Arasteh, J.M., Mayer, U.,
859 Carding, S.R., Wileman, T., Beale, R., and Florey, O. (2018). The WD40 domain of
860 ATG16L1 is required for its non-canonical role in lipidation of LC3 at single membranes.
861 EMBO J *37*. 10.15252/embj.201797840.
862 113. Popovic, D., Akutsu, M., Novak, I., Harper, J.W., Behrends, C., and Dikic, I. (2012). Rab
863 GTPase-activating proteins in autophagy: regulation of endocytic and autophagy
864 pathways by direct binding to human ATG8 modifiers. Molecular and cellular biology *32*,
865 1733-1744. 10.1128/MCB.06717-11.
866 114. Borchers, A.C., Langemeyer, L., and Ungermann, C. (2021). Who's in control? Principles
867 of Rab GTPase activation in endolysosomal membrane trafficking and beyond. J Cell Biol
868 *220*. 10.1083/jcb.202105120.
869 115. Stroupe, C. (2018). This Is the End: Regulation of Rab7 Nucleotide Binding in
870 Endolysosomal Trafficking and Autophagy. Front Cell Dev Biol *6*, 129.
871 10.3389/fcell.2018.00129.
872 116. Zhen, Y., Radulovic, M., Vietri, M., and Stenmark, H. (2021). Sealing holes in cellular
873 membranes. EMBO J *40*, e106922. 10.15252/embj.2020106922.
874 117. Kumar, S., Jia, J., and Deretic, V. (2021). Atg8ylation as a general membrane stress and
875 remodeling response. Cell Stress *5*, 128-142. 10.15698/cst2021.09.255.
876 118. Seaman, M.N. (2007). Identification of a novel conserved sorting motif required for
877 retromer-mediated endosome-to-TGN retrieval. J Cell Sci *120*, 2378-2389.
878 10.1242/jcs.009654.
879 119. Simonetti, B., Danson, C.M., Heesom, K.J., and Cullen, P.J. (2017). Sequence-dependent
880 cargo recognition by SNX-BARs mediates retromer-independent transport of CI-MPR. J
881 Cell Biol *216*, 3695-3712. 10.1083/jcb.201703015.

882 120. Kvainickas, A., Jimenez-Orgaz, A., Nagele, H., Hu, Z., Dengjel, J., and Steinberg, F. (2017).
883 Cargo-selective SNX-BAR proteins mediate retromer trimer independent retrograde
884 transport. J Cell Biol *216*, 3677-3693. 10.1083/jcb.201702137.
885 121. Buser, D.P., Bader, G., and Spiess, M. (2022). Retrograde transport of CDMPR depends
886 on several machineries as analyzed by sulfatable nanobodies. Life Sci Alliance *5*.
887 10.26508/lsa.202101269.
888 122. Seaman, M.N.J., Mukadam, A.S., and Breusegem, S.Y. (2018). Inhibition of TBC1D5
889 activates Rab7a and can enhance the function of the retromer cargo-selective complex.
890 J Cell Sci *131*. 10.1242/jcs.217398.
891 123. Behrends, C., Sowa, M.E., Gygi, S.P., and Harper, J.W. (2010). Network organization of
892 the human autophagy system. Nature *466*, 68-76. nature09204 [pii]
893 10.1038/nature09204.
894 124. Yamano, K., Fogel, A.I., Wang, C., van der Bliek, A.M., and Youle, R.J. (2014).
895 Mitochondrial Rab GAPs govern autophagosome biogenesis during mitophagy. Elife *3*,
896 e01612. 10.7554/eLife.01612.
897 125. Jia, D., Zhang, J.S., Li, F., Wang, J., Deng, Z.H., White, M.A., Osborne, D.G., Phillips-
898 Krawczak, C., Gomez, T.S., Li, H.Y., et al. (2016). Structural and mechanistic insights into
899 regulation of the retromer coat by TBC1d5. Nature Communications *7*. ARTN 13305
900 10.1038/ncomms13305.
901
902

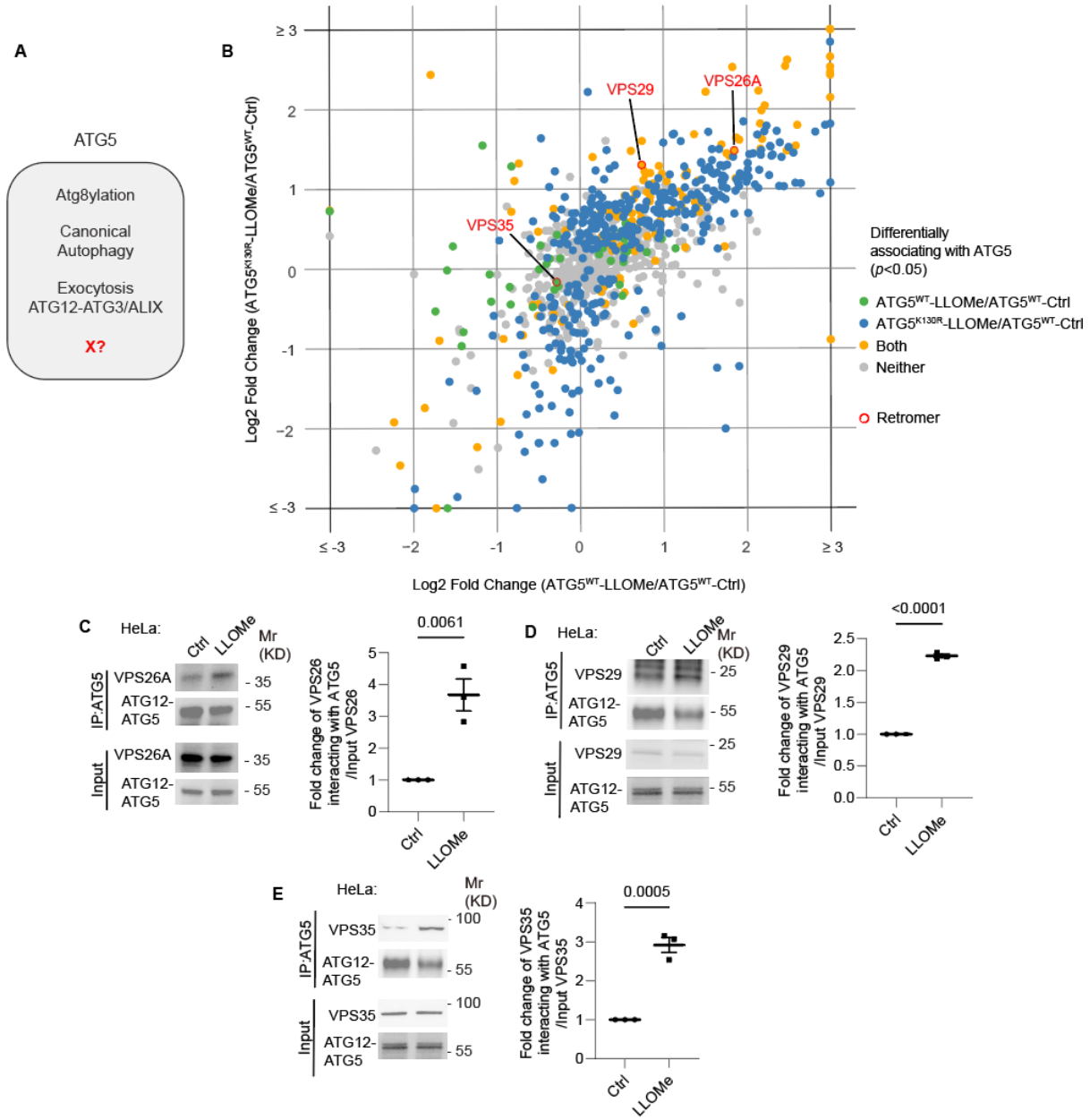

Figure 1: ATG5 interacts with retromer. A. ATG5 functions. X, a postulated additional function. **B.** 2D scatter plot (log2 fold changes; color coded p value cutoff matrix for comparisons between samples as per the lookup table) of proximity biotinylation LC/MS/MS datasets: FlpIn-HeLa$^{APEX2\text{-}ATG5\text{-}WT}$ cells (X-axis) and FlpIn-HeLa$^{APEX2\text{-}ATG5\text{-}K130R}$ (Y-axis) treated with 2 mM LLOMe for 30 min ratioed vs. HeLa$^{APEX2\text{-}ATG5\text{-}WT}$ without LLOMe treatment (Ctrl). **C-E.** Co-IP analyses and quantification of VPS26A (C), VPS29 (D) VPS35, (E), interaction with ATG5 in HeLa cells treated with or without 2 mM

LLOMe for 30 min. Data, means ± SE (n=3); unpaired *t*-test; p values indicated above the bars.

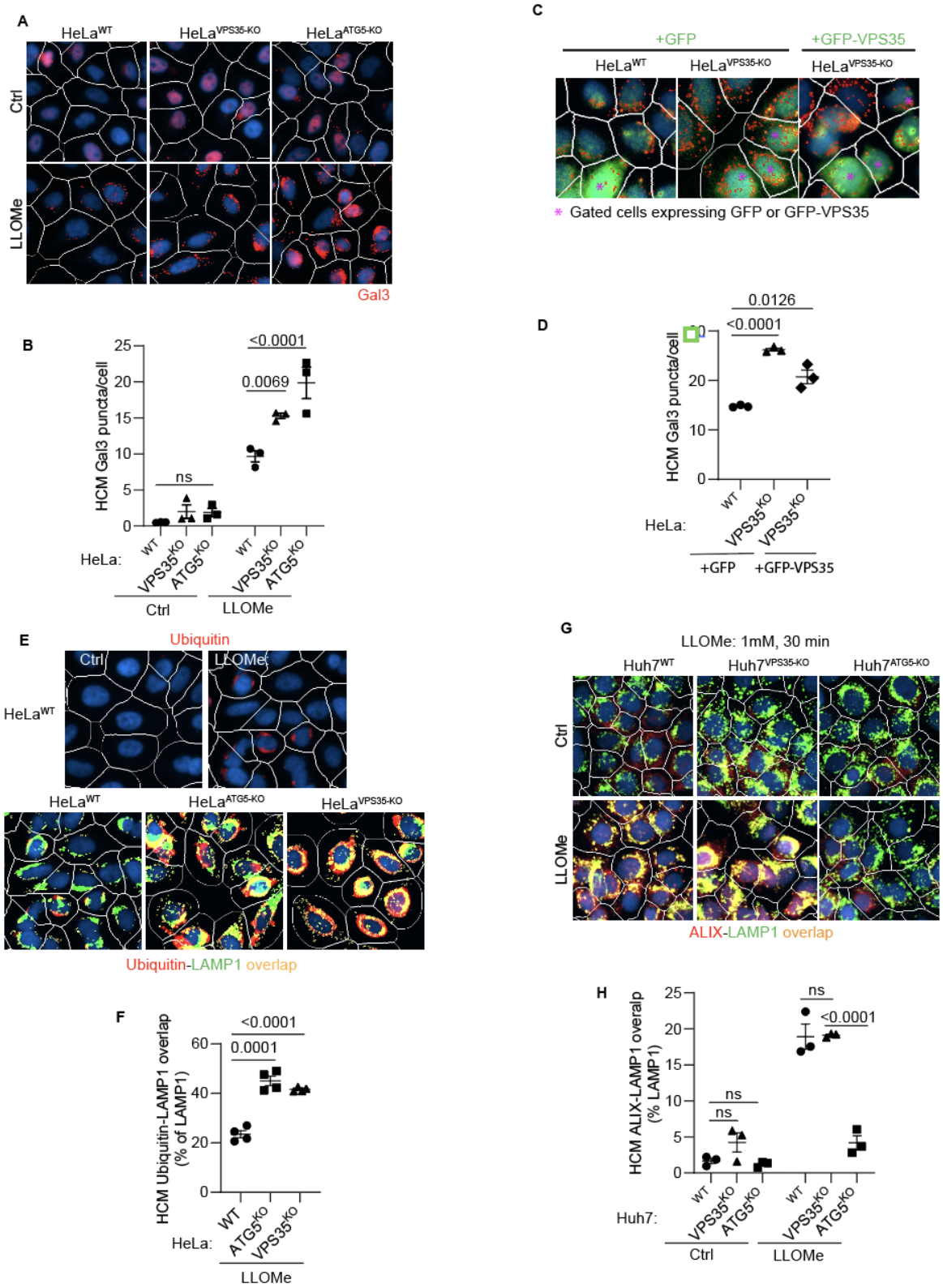

Figure 2: Retromer affects lysosomal sensitivity to damage. A,B. High content microscopy (HCM) imaging and quantification of Gal3 response (puncta/cell of

endogenous Gal3 profiles stained for immunofluorescence) in HeLa^{WT}, HeLa$^{ATG5\text{-}KO}$, and HeLa$^{VPS35\text{-}KO}$ cells subjected to lysosomal damage by Leu-Leu-O-Me ester hydrobromide (LLOMe; 2mM, 30 min). HCM, an unbiased machine-driven image acquisition and data analysis based on presets of >500 valid primary objects/cells per well (representative images shown; white mask, cell; red masks, Gal3 puncta), with a minimum of 5 wells per sample (sampling error), and n≥3, independent biological replicates (experimental error) in separate 96-well plates. Data, means ± SE (n=3), two-way ANOVA with Tukey's multiple comparisons. **C,D**. Complementation analysis of VPS35^{KO} LyHYP (lysosome hypersensitivity) phenotype monitored by HCM quantification of Gal3 puncta in HeLa$^{VPS35\text{-}KO}$ cells transfected with GFP (control) or GFP-VPS35 expressing plasmids. Data, means ± SE (n=3); one-way ANOVA with Tukey's multiple comparisons. **E,F.** Comparative HCM analysis of ubiquitin (immunofluorescence; FK2 antibody) response to lysosomal damage (LLOMe; 2mM, 30 min) in HeLa$^{ATG5\text{-}KO}$ and HeLa$^{VPS35\text{-}KO}$ cells. Yellow profiles, colocalization of ubiquitin and LAMP1. Top panels, ubiquitin immunostaining alone. Data, means ± SE (n=4), two-way ANOVA with Tukey's multiple comparisons. **G,H.** HCM quantification of ALIX localization to endolysosomal compartments (% of LAMP1 profiles positive for ALIX immunostaining) in Huh7^{WT}, Huh7$^{ATG5\text{-}KO}$, and Huh7$^{VPS35\text{-}KO}$ cells following lysosomal damage. Yellow profiles, colocalization of ALIX and LAMP1. Data, means ± SE (n=3); two-way ANOVA with Tukey's multiple comparisons. HCM images in all relevant panels, examples from a bank of unbiased operator-independent machine-collected and algorithm-processed fields containing a minimum of 500 primary objects/cells per well (5 wells minimum per 96-well plate; 3 plates minimum), per cell line/condition.

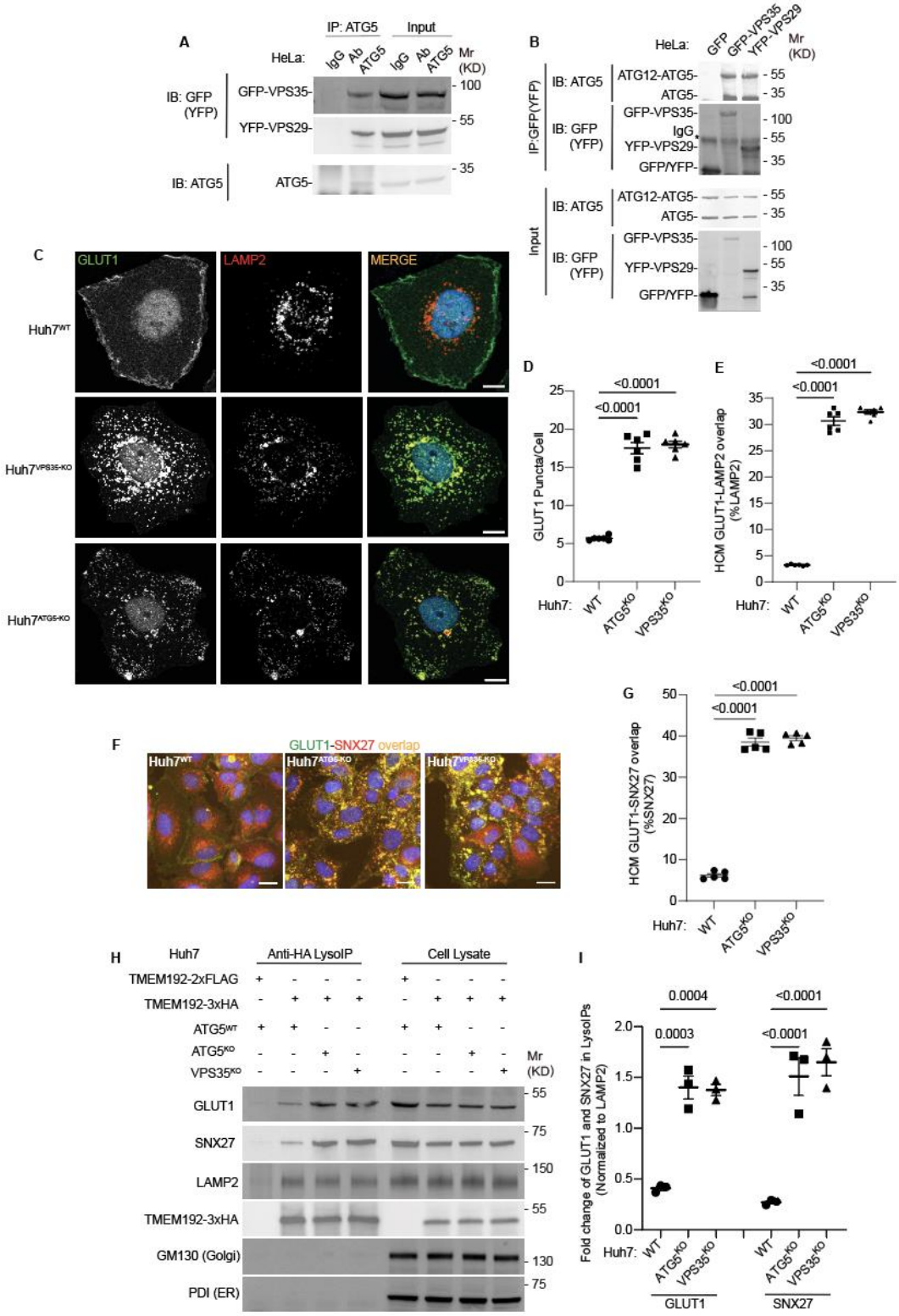

Figure 3: ATG5 affects sorting of the retromer cargo GLUT1. A. Co-IP analysis of endogenous ATG5 with GFP-VPS35 or YFP-VPS29 (transient transfection). **B.** Reverse

Co-IP analysis GFP-VPS35 or YFP-VPS29 (transient transfection) and endogenous ATG5. **C.** Confocal images illustrating localization of GLUT1 and LAMP2 in Huh7^{WT}, Huh7$^{VPS35\text{-}KO}$, and Huh7$^{ATG5\text{-}KO}$ cells. Scale bar, 10 µm. **D,E.** HCM quantification of GLUT1 (endogenous protein immunostaining) puncta/cell (D) and GLUT1 colocalization with LAMP2 (% of LAMP2 profiles positive for GLUT1; overlap area) (E) in Huh7^{WT}, Huh7$^{ATG5\text{-}KO}$, and Huh7$^{VPS35\text{-}KO}$ cells. Scale bar, 20 µm. Data, means ± SE (n =6); one-way ANOVA with Tukey's multiple comparisons. **F,G.** HCM quantification of GLUT1-SNX27 overlap (% of SNX7 area positive for GLUT1) in Huh7^{WT}, Huh7$^{ATG5\text{-}KO}$, and Huh7$^{VPS35\text{-}KO}$ cells. Scale bar, 20 µm. Data, means ± SE (n=5); one-way ANOVA with Tukey's multiple comparisons. **H,I.** Immunoblot analysis and quantification of proteins in lysosomes purified/enriched by LysoIP (immunoisolation with TMEM192-3xHA) from Huh7^{WT}, Huh7$^{ATG5\text{-}KO}$, and Huh7$^{VPS35\text{-}KO}$ cells. TMEM192-2xFLAG, negative control. Data, means ± SE (n=3), one-way ANOVA with Tukey's multiple comparisons. HCM images in panel F, examples from a bank of unbiased operator-independent machine-collected and algorithm-processed fields containing a minimum of 500 primary objects/cells per well (5 wells minimum per 96-well plate; 3 plates minimum), per cell line.

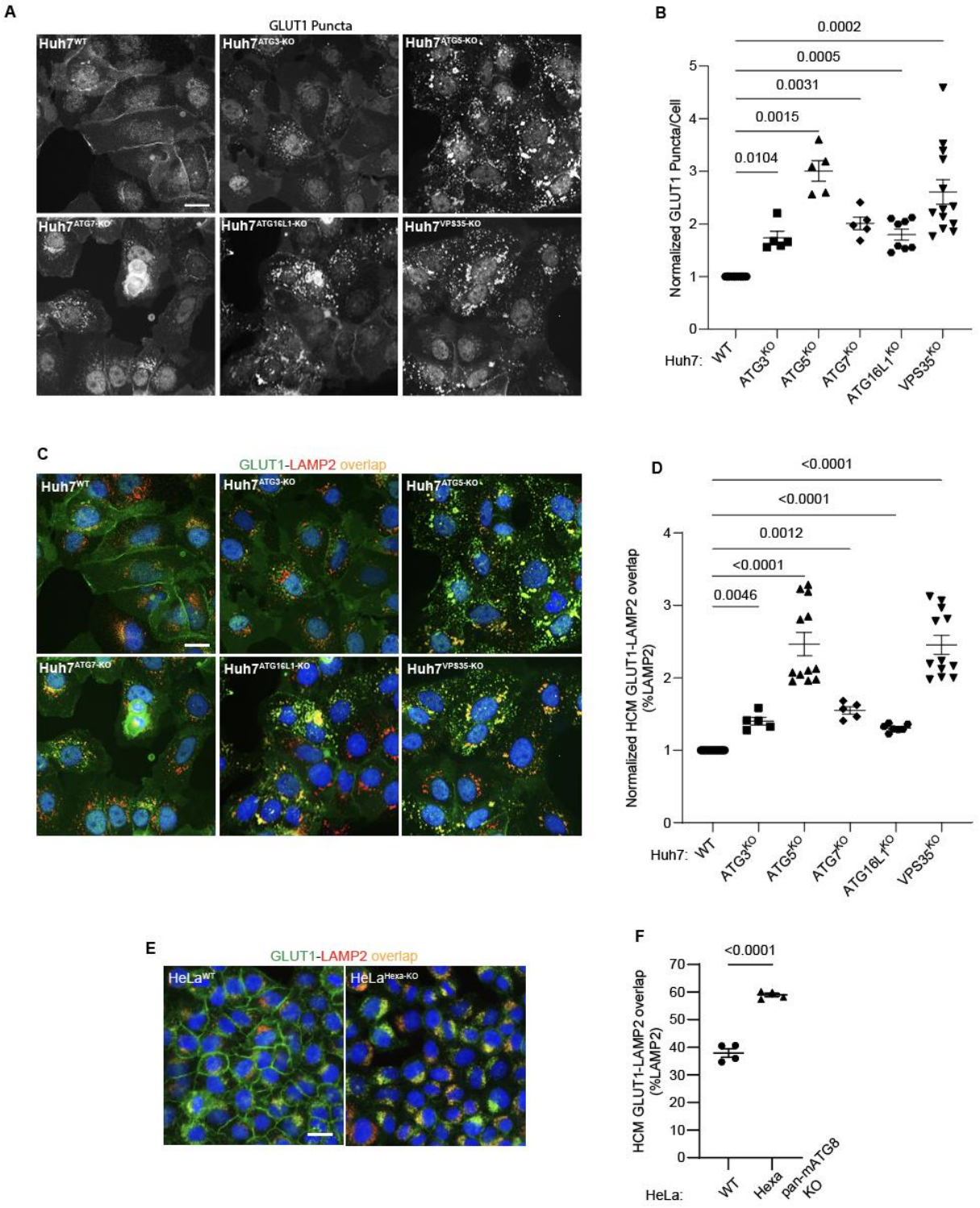

Figure 4: Membrane atg8ylation apparatus affects sorting of the retromer cargo GLUT1. A,B. HCM quantification of GLUT1 (endogenous protein immunostaining) puncta/cell in Huh7^{WT}, Huh7$^{ATG3\text{-}KO}$, Huh7$^{ATG5\text{-}KO}$, Huh7$^{ATG7\text{-}KO}$, Huh7$^{ATG16\text{-}KO}$, and

Huh7$^{VPS35\text{-}KO}$ cells. Scale bar, 20 μm. Data, means ± SE (n=5); one-way ANOVA with Tukey's multiple comparisons. **C,D.** HCM quantification of GLUT1 (endogenous protein immunostaining) colocalization with LAMP2 (% of LAMP2 profiles positive for GLUT1; overlap area) in Huh7^{WT}, Huh7$^{ATG3\text{-}KO}$, Huh7$^{ATG5\text{-}KO}$, Huh7$^{ATG7\text{-}KO}$, Huh7$^{ATG16\text{-}KO}$, and Huh7$^{VPS35\text{-}KO}$ cells. Scale bar, 20 μm. Data, means ± SE (n=5); one-way ANOVA with Tukey's multiple comparisons. **E,F.** HCM quantification of GLUT1 (endogenous protein immunostaining) colocalization with LAMP2 (% of LAMP2 profiles positive for GLUT1; overlap area) in HeLa^{WT}, and HeLa$^{Hexa\text{-}KO}$ cells. Scale bar, 20 μm. Data, means ± SE (n=5); one-way ANOVA with Tukey's multiple comparisons. HCM images in all relevant panels, examples from a bank of unbiased operator-independent machine-collected and algorithm-processed fields containing a minimum of 500 primary objects/cells per well (5 wells minimum per 96-well plate; 3 plates minimum), per cell line.

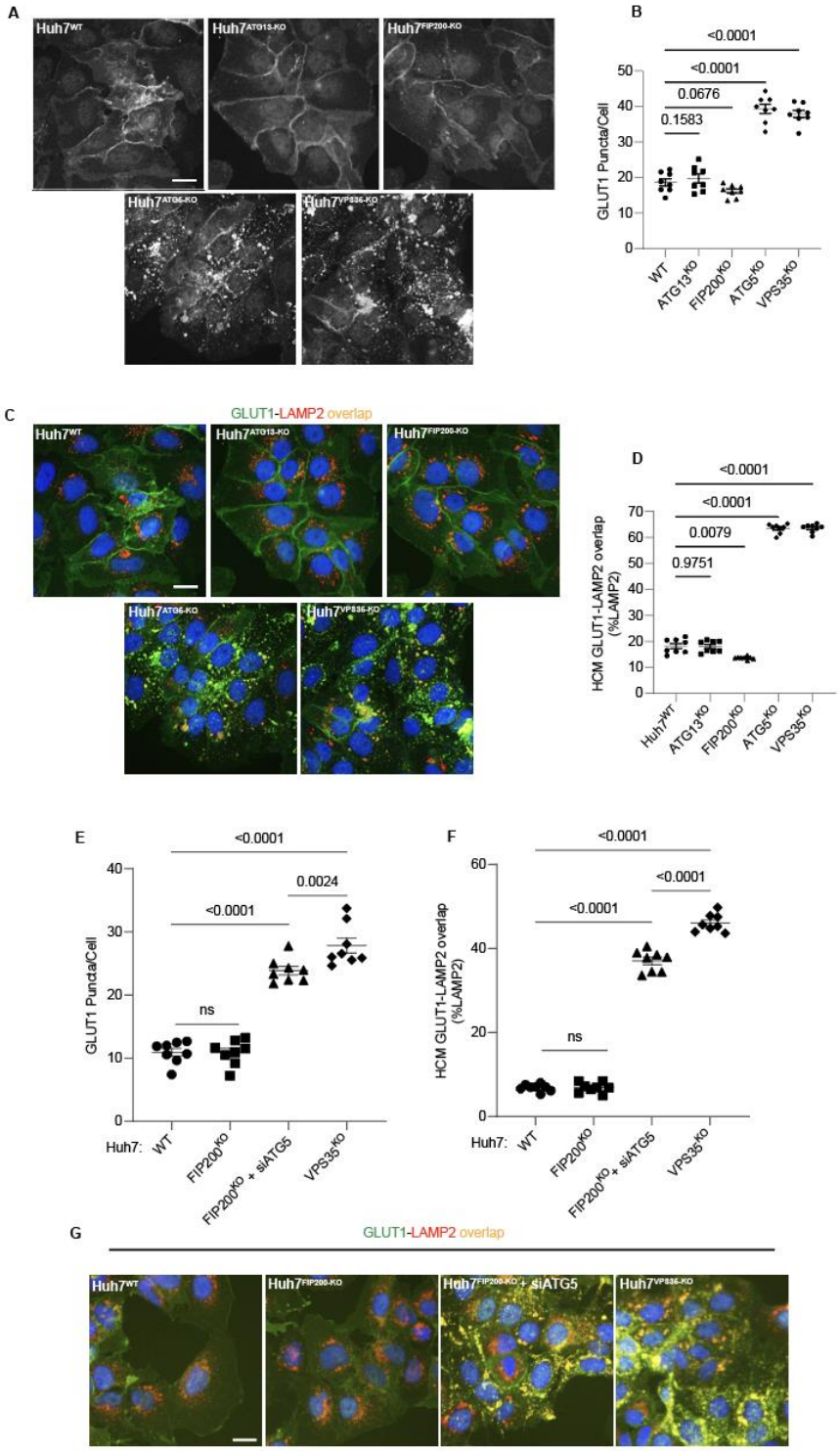

Figure 5: Canonical autophagy does not affect sorting of the retromer cargo GLUT1. A,B. HCM quantification of GLUT1 (immunostaining of endogenous protein) puncta/cell in in Huh7^{WT}, Huh7$^{ATG13\text{-}KO}$, Huh7$^{FIP200\text{-}KO}$, Huh7$^{ATG5\text{-}KO}$, and Huh7$^{VPS35\text{-}KO}$

cells. Scale bar, 20 µm. Data, means ± SE (n=5); one-way ANOVA with Tukey's multiple comparisons. **C,D.** HCM quantification of GLUT1 (immunostaining of endogenous protein) colocalization with LAMP2 (% of LAMP2 profiles positive for GLUT1; overlap area) in in Huh7^{WT}, Huh7$^{ATG13\text{-}KO}$, Huh7$^{FIP200\text{-}KO}$, Huh7$^{ATG5\text{-}KO}$, and Huh7$^{VPS35\text{-}KO}$ cells. Scale bar, 20 µm. Data, means ± SE (n=5); one-way ANOVA with Tukey's multiple comparisons. **E-G.** HCM quantification of GLUT1 (immunostaining of endogenous protein) puncta/cell (E) and GLUT1 colocalization with LAMP2 (% of LAMP2 profiles positive for GLUT1; overlap area) (F) in Huh7^{WT}, Huh7$^{FIP200\text{-}KO}$, Huh7$^{FIP200\text{-}KO + siATG5}$, and Huh7$^{VPS35\text{-}KO}$ cells. Scale bar, 20 µm. Data, means ± SE (n =6); one-way ANOVA with Tukey's multiple comparisons. HCM images in all relevant panels, examples from a bank of unbiased operator-independent machine-collected and algorithm-processed fields containing a minimum of 500 primary objects/cells per well (5 wells minimum per 96-well plate; 3 plates minimum), per cell line.

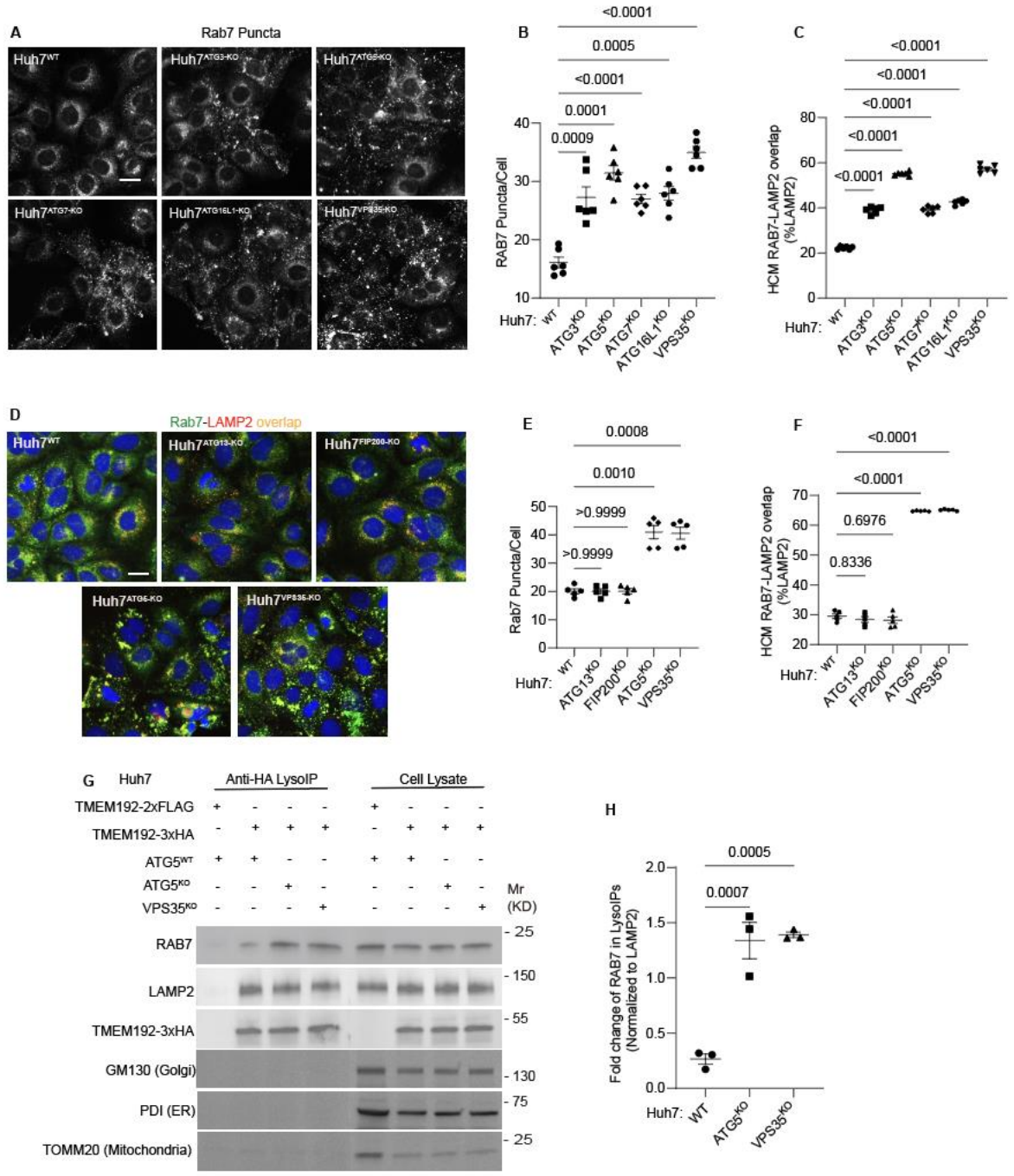

Figure 6: Membrane atg8ylation machinery is required for proper RAB7 localization.

A-C HCM quantification of Rab7 (endogenous protein immunostaining) puncta/cell (B) and Rab7 colocalization with LAMP2 (% of LAMP2 profiles positive for GLUT1; overlap area) (C) in Huh7^{WT}, Huh7$^{ATG3\text{-}KO}$, Huh7$^{ATG5\text{-}KO}$, Huh7$^{ATG7\text{-}KO}$, Huh7$^{ATG16\text{-}KO}$, and

Huh7$^{VPS35\text{-}KO}$ cells. Scale bar, 20 µm. Data, means ± SE (n =6); one-way ANOVA with Tukey's multiple comparisons. **D-F.** HCM quantification of Rab7 (endogenous protein immunostaining) puncta/cell (E) and Rab7 colocalization with LAMP2 (% of LAMP2 profiles positive for GLUT1; overlap area) (F) in Huh7^{WT}, Huh7$^{ATG13\text{-}KO}$, Huh7$^{FIP200\text{-}KO}$, Huh7$^{ATG5\text{-}KO}$, and Huh7$^{VPS35\text{-}KO}$ cells. Scale bar, 20 µm. Data, means ± SE (n =6); one-way ANOVA with Tukey's multiple comparisons. **G,H.** Immunoblot analysis and quantification of proteins in lysosomes purified/enriched by LysoIP (immunoisolation with TMEM192-3xHA) from Huh7^{WT}, Huh7$^{ATG5\text{-}KO}$, and Huh7$^{VPS35\text{-}KO}$ cells. TMEM192-2xFLAG, negative control. Data, means ± SE (n=3), one-way ANOVA with Tukey's multiple comparisons. HCM images in all relevant panels, examples from a bank of unbiased operator-independent machine-collected and algorithm-processed fields containing a minimum of 500 primary objects/cells per well (5 wells minimum per 96-well plate; 3 plates minimum), per cell line.

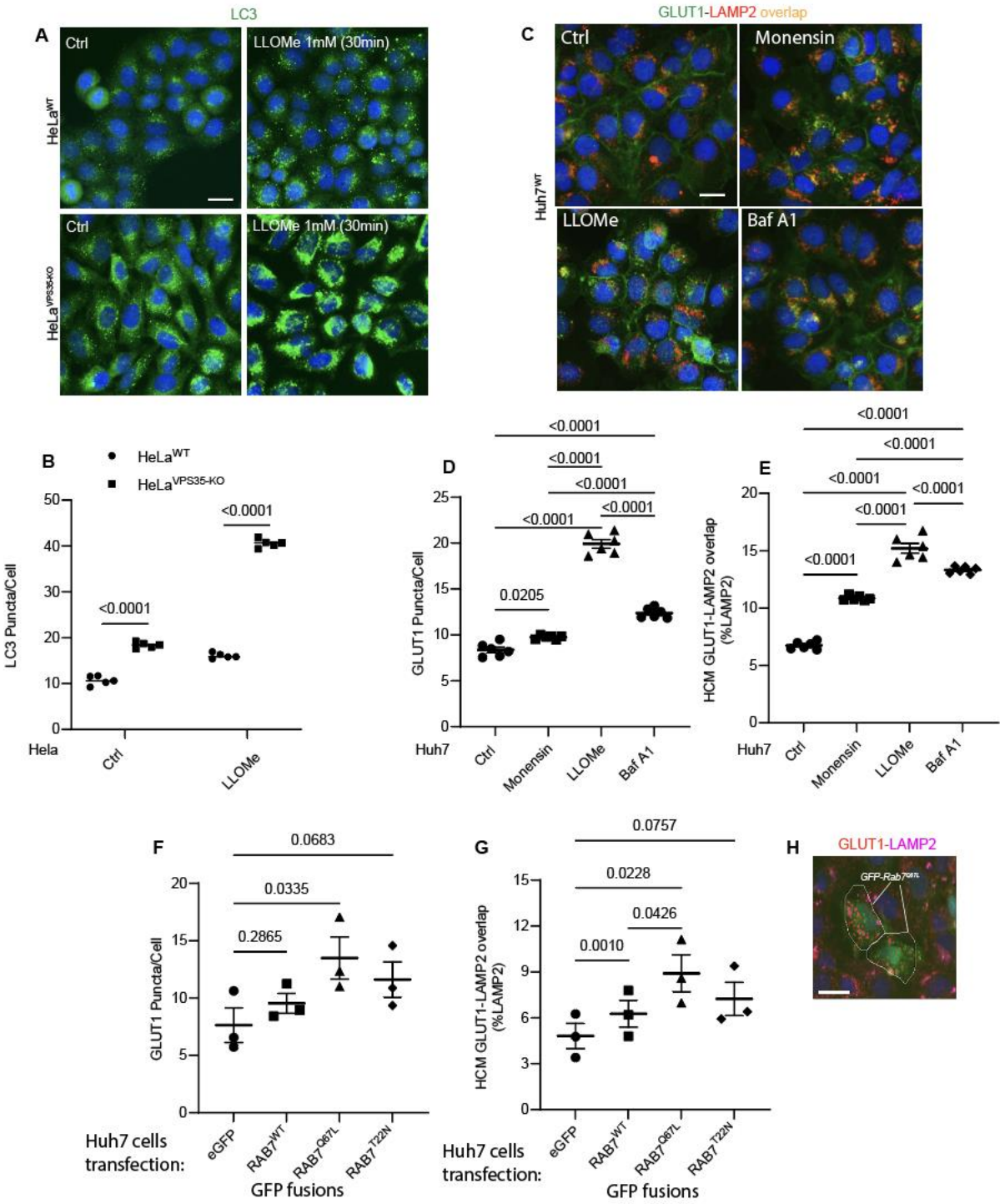

Figure 7: CASM induction affects sorting of the retromer cargo GLUT1. A,B. HCM imaging and quantification of LC3 response (puncta/cell of endogenous LC3 immunofluorescent profiles) in HeLa^{WT}, and HeLa$^{VPS35\text{-}KO}$ cells in response to lysosomal damage by LLOMe (1mM, 30 and 60 min). Scale bar, 20 µm. Data, means ± SE (n=5),

one-way ANOVA with Tukey's multiple comparisons. **C-E.** HCM quantification of GLUT1 response (puncta/cell of endogenous GLUT1, D) and its localization to endolysosomal compartments (% of LAMP1 profiles positive for GLUT1 immunostaining, E) in Huh7^{WT} treated with or without Monensin (100µM), LLOMe (100µM), and Bafilomycin A1 (100nM) for 45 minutes. Scale bar, 20 µm. Data, means ± SE (n=5), one-way ANOVA with Tukey's multiple comparisons. F-H. Analysis of GLUT1 puncta/cell (F) and its localization to endolysosomal compartments (% of LAMP1 profiles positive for GLUT1 immunostaining, G) phenotype monitored by HCM quantification in Huh7^{WT} cells transfected with GFP (control) or GFP-Rab7^{WT}, GFP-Rab7^{Q67L}, and GFP-Rab7^{T22N}, expressing plasmids. Scale bar, 20 µm. Data, means ± SE (n=3); one-way ANOVA with Tukey's multiple comparisons. HCM images in all relevant panels, examples from a bank of unbiased operator-independent machine-collected and algorithm-processed fields containing a minimum of 500 primary objects/cells per well (5 wells minimum per 96-well plate; 3 plates minimum), per cell line/condition.

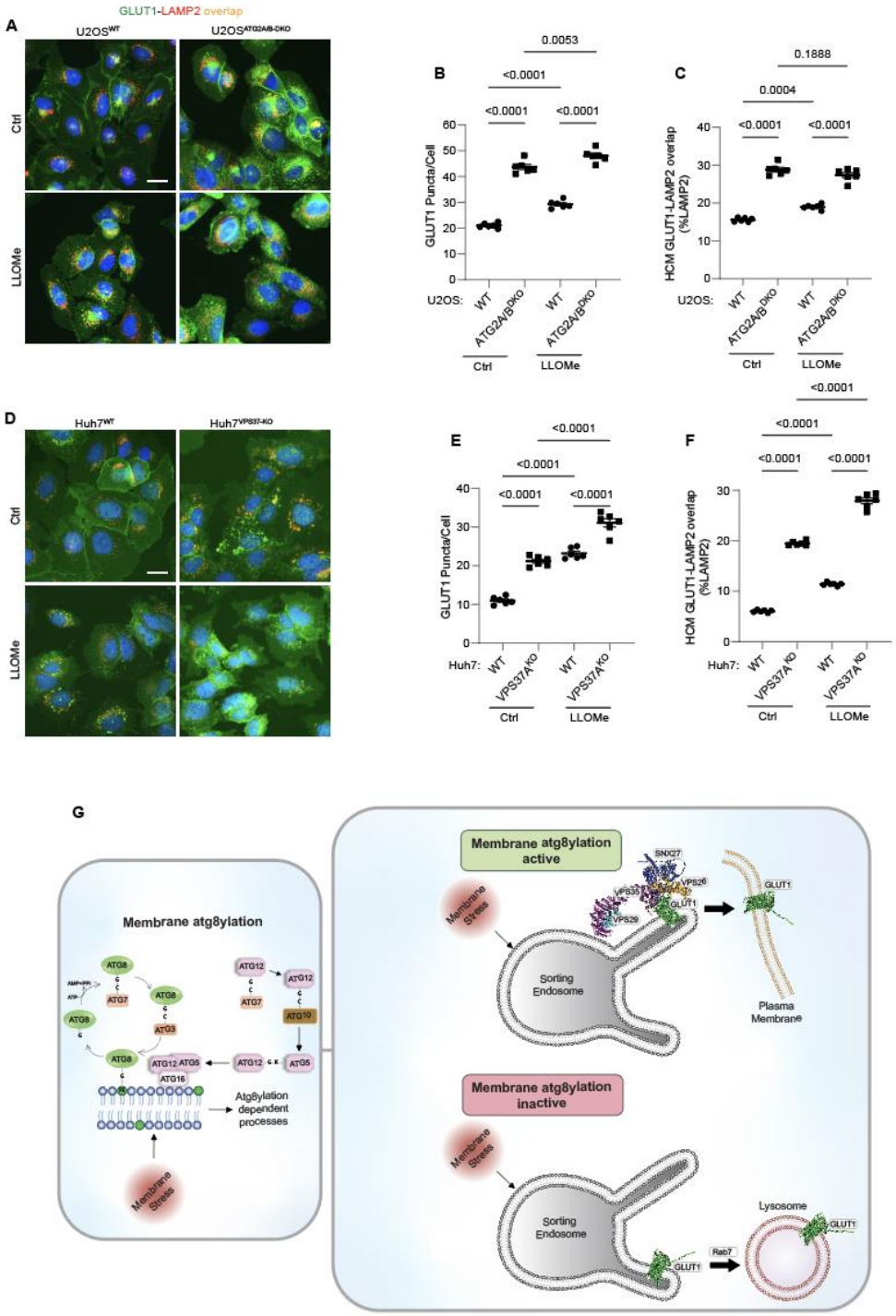

Figure 8: Membrane atg8ylation and endolysosomal homeostasis affect retromer-dependent sorting. A-C. HCM quantification of GLUT1 (immunostaining of endogenous protein) puncta/cell (B) and GLUT1 colocalization with LAMP2 (% of

LAMP2 profiles positive for GLUT1; overlap area, C) in U2OS^{WT} and U2OS$^{ATG2A/B\text{-}DKO}$ cells treated with or without LLOMe (100µM) for 45 minutes. Scale bar, 20 µm. Data, means ± SE (n =6); one-way ANOVA with Tukey's multiple comparisons. **D-F.** HCM quantification of GLUT1 (immunostaining of endogenous protein) puncta/cell (E) and GLUT1 colocalization with LAMP2 (% of LAMP2 profiles positive for GLUT1; overlap area, F) in Huh7^{WT} cand Huh7$^{VPS37A\text{-}KO}$ cells treated with or without LLOMe (100µM) for 45 minutes. Scale bar, 20 µm. Data, means ± SE (n =6); one-way ANOVA with Tukey's multiple comparisons. HCM images in all relevant panels, examples from a bank of unbiased operator-independent machine-collected and algorithm-processed fields containing a minimum of 500 primary objects/cells per well (5 wells minimum per 96-well plate; 3 plates minimum), per cell line/condition. **G.** Schematic: Membrane atg8ylation maintains membrane homeostasis under basal or stress conditions and, independently of canonical autophagy, affects retromer function under. A functional atg8ylation apparatus is required for proper sorting of the retromer cargo GLUT1.

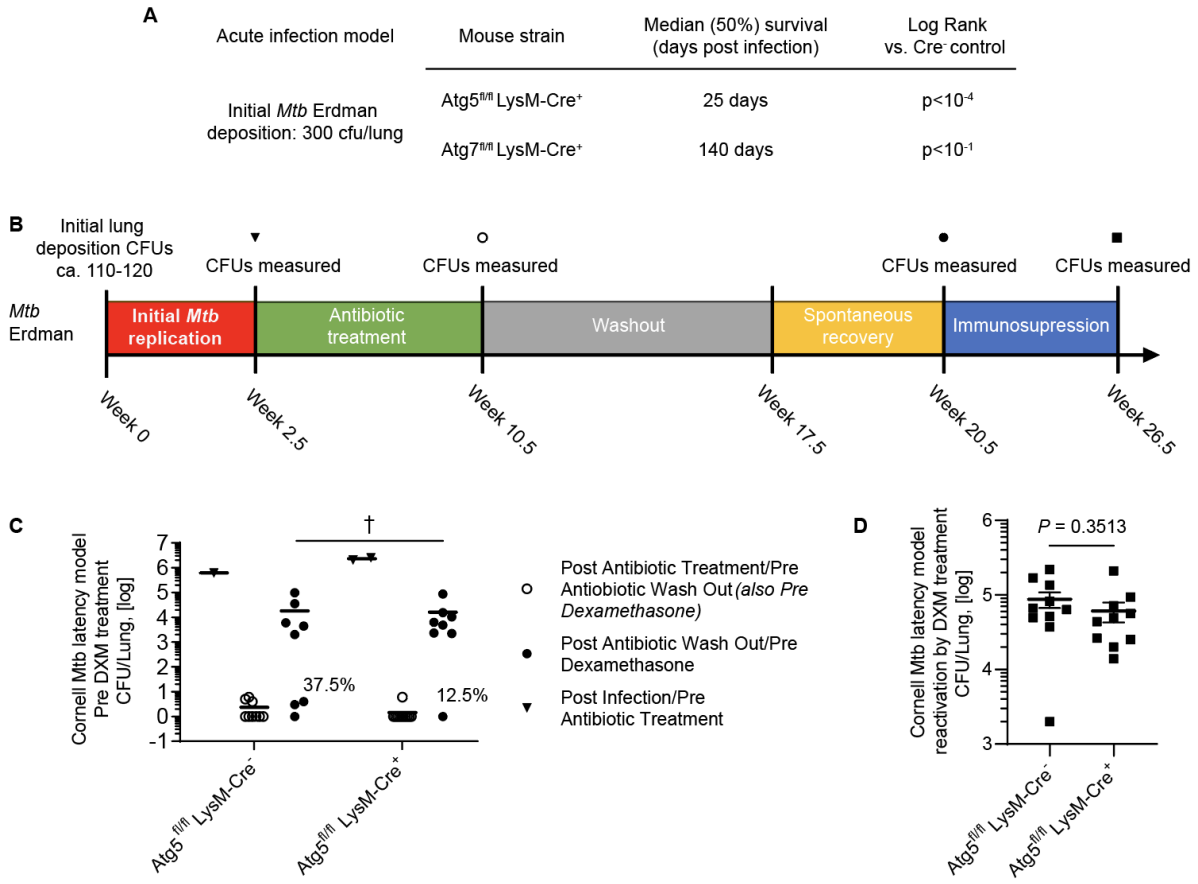

Supplementary Figure S1. Cornell model of *M. tuberculosis* latent infection in mice and effects of Atg5 loss in myeloid lineage on disease reactivation. A. Summary of mice mortality data in acute infection model of *Mtb* infection (aerosol) based on survival curves in ref. 35. **B.** Details and timeline of the Cornell latency model experiments (see narrative in Methods). **C.** Effects of Atg5 loss on spontaneous reactivation of *M. tuberculosis* infection in Atg5$^{fl/fl}$ LysM-Cre^{+} mice (loss of Atg5 in myeloid lineage) vs. Atg5$^{fl/fl}$ LysM-Cre^{-} (control) mice. Mice were infected with an aerosol of *M. tuberculosis* (initial deposition, 100-120 CFUs per lung). After a period of 2.5 weeks, initial bacterial growth was assessed by determining lung CFUs (triangles), mice were treated PO with antibiotics (0.1g/L INH and 0.15g/L RIF in drinking water) for 8 weeks, bacterial clearance after chemotherapy assessed by determining lung CFUs (open circles), and remaining mice subjected to antibiotic washout for 7 weeks plus spontaneous reactivation period with no treatment of 3 weeks at which time the mice were sacrificed and lung CFUs determined by plating (filled circles). Data and statistics

for spontaneous reactivation: means, †p≥0.05, *t* test; n=8 mice per group. **D.** Cornell murine model of *M. tuberculosis* latent infection and dexamethasone (DXM) induced reactivation and effects of Atg5 loss in myeloid lineage of $Atg5^{fl/fl}$ LysM-Cre^{+} mice (vs. $Atg5^{fl/fl}$ LysM-Cre^{-} control mice). Mice were infected with *M. tuberculosis* aerosols (initial lung deposition 100-120 CFUs), bacteria allowed to replicate in vivo, mice subjected to antibiotic regimen, followed by antibiotic washout period, after which immunosuppression with DXM was carried out to reactivate infection/bacterial replication (details in Methods). Data, CFU's per mouse lungs (means ± SE, *t* test, n=10 mice per group).

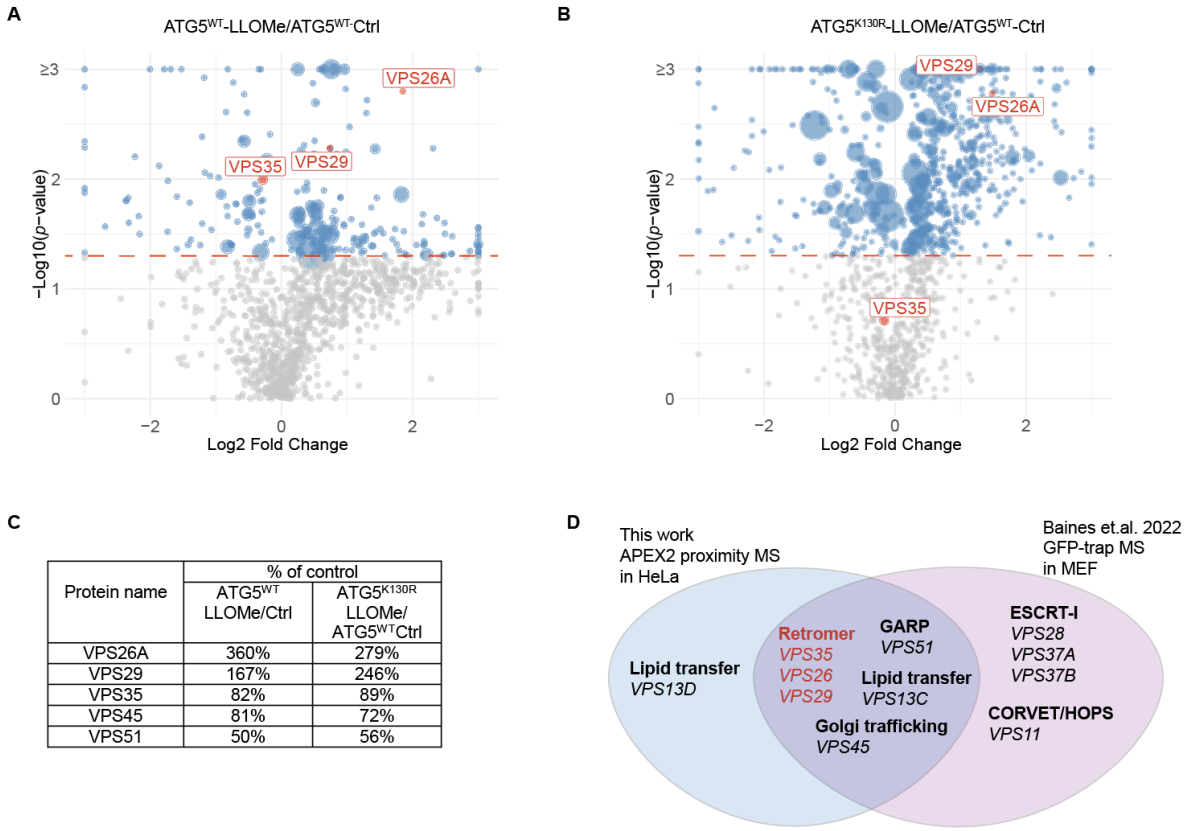

C

Protein name	% of control	
	ATG5^{WT} LLOMe/Ctrl	ATG5^{K130R} LLOMe/ ATG5^{WT}Ctrl
VPS26A	360%	279%
VPS29	167%	246%
VPS35	82%	89%
VPS45	81%	72%
VPS51	50%	56%

E APEX2-SGALS1

LLOMe/Ctrl	
Retromer subunit	% of control
VPS26A	67%
VPS29	102%
VPS35	101%

Supplementary Figure S2. ATG5 interactome analysis. A. Volcano plot of proximity biotinylation LC-MS/MS interactome comparing FlpIn-HeLa$^{APEX2\text{-}ATG5\text{-}WT}$ treated with or without 2 mM LLOMe for 30 min. Diameter of symbols reflects relative number of unique peptides identified. **B**. Volcano plot of proximity biotinylation LC-MS/MS interactome comparing FlpIn-HeLa$^{APEX2\text{-}ATG5\text{-}K130R}$ treated with 2 mM LLOMe for 30 min and FlpIn-HeLa$^{APEX2\text{-}ATG5\text{-}WT}$ without LLOMe treatment. **C**. VPS proteins in the MS DIA data. **D.** VPS proteins identified here compared to VPS proteins in Ref. 86. **E.** Table: Control MS data (APEX2-SGALS1) for comparison with data in panel C; note no increase in retromer subunits with LLOMe treatment in the APEX1-SGALS1 dataset.

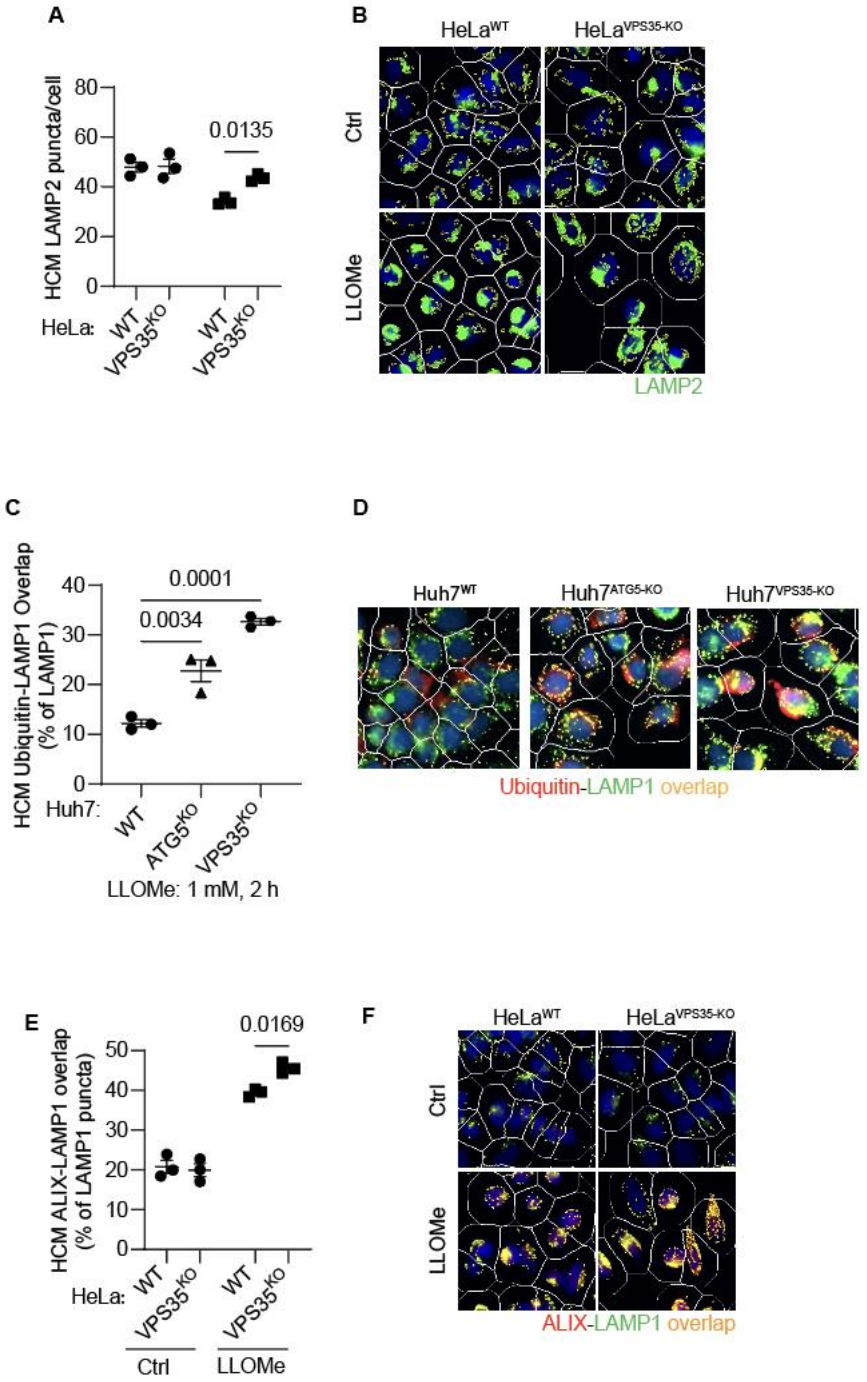

Supplementary Figure S3. Retromer affects a subset of responses to lysosomal damage. A,B. HCM imaging and quantification of LC3 (puncta/cell of immunofluorescently stained endogenous LC3 profiles) in HeLa^{WT}, and HeLa$^{VPS35\text{-}KO}$ cells in response to lysosomal damage by LLOMe. Data, means ± SE (n=3), one-way ANOVA with Tukey's multiple comparisons. **C,D**. HCM analysis of ubiquitin

(immunofluorescence; FK2 antibody) response to lysosomal damage (LLOMe; 1mM, 2 h) in Huh7^{WT}, Huh7$^{ATG5\text{-}KO}$, and Huh7$^{VPS35\text{-}KO}$ cells. Yellow profiles, colocalization of ubiquitin and LAMP1. Data, means ± SE (n=3), one-way ANOVA with Tukey's multiple comparisons. **E,F.** HCM quantification of ALIX localization to endolysosomal compartments (% of LAMP1 profiles positive for ALIX immunostaining) in HeLa^{WT} and HeLa$^{VPS35\text{-}KO}$ cells following lysosomal damage. Yellow profiles, colocalization of ALIX and LAMP1. Data, means ± SE (n=3); two-way ANOVA with Tukey's multiple comparisons. HCM images in all relevant panels, examples from a bank of unbiased operator-independent machine-collected and algorithm-processed fields containing a minimum of 500 primary objects/cells per well (5 wells minimum per 96-well plate; 3 plates minimum), per cell line/condition.

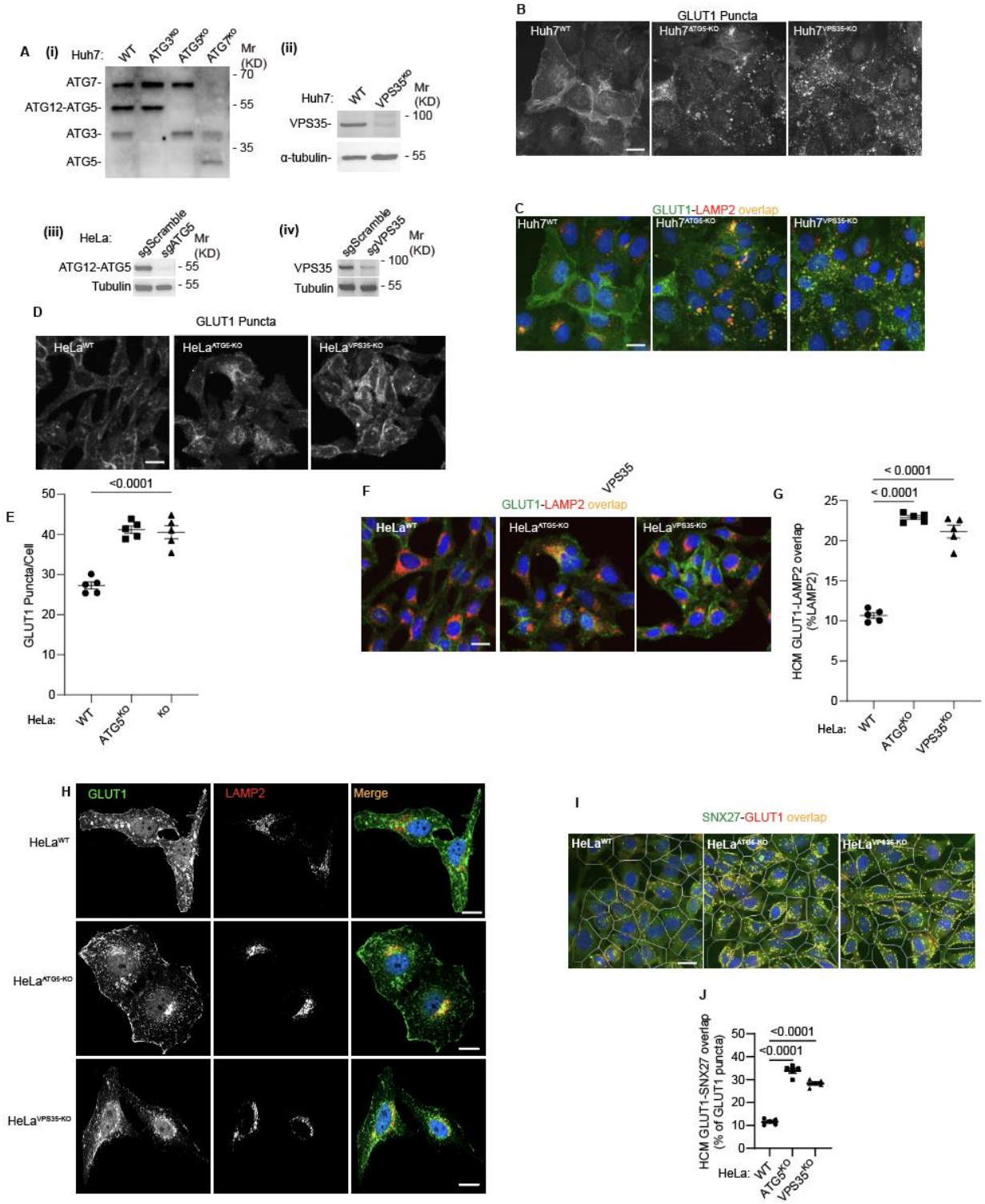

Supplementary Figure S4. Membrane atg8ylation regulates retromer function. A. Immunoblots of CRISPR KOs: (i) ATG3, ATG5, and ATG7 in Huh7 cells; (ii) VPS35 in Huh7 cells; (iii) ATG5 in HeLa cells; and (iv) VPS35 in Hela cells. **B,C.** HCM images

(example form a bank of unbiased operator-independent machine collected and processed images containing a minimum of 500 primary objects/cells) of GLUT1 (immunostaining of endogenous protein) puncta/cell (B) and GLUT1 colocalization with LAMP2 in Huh7^{WT}, Huh7$^{ATG5\text{-}KO}$, and Huh7$^{VPS35\text{-}KO}$ cells (C). Scale bar, 20 µm. **D,E.** HCM quantification of GLUT1 (immunostaining of endogenous protein) puncta/cell in HeLa^{WT}, HeLa$^{ATG5\text{-}KO}$, and HeLa$^{VPS35\text{-}KO}$ cells. Scale bar, 20 µm. Data, means ± SE (n =5); one-way ANOVA with Tukey's multiple comparisons. **F,G.** HCM quantification of GLUT1 colocalization with LAMP2 (% of LAMP2 profiles positive for GLUT1; overlap area) in HeLa^{WT}, HeLa$^{ATG5\text{-}KO}$, and HeLa$^{VPS35\text{-}KO}$ cells. Scale bar, 20 µm. Data, means ± SE (n =5); one-way ANOVA with Tukey's multiple comparisons. **H.** Confocal images illustrating localization of GLUT1 and LAMP2 in HeLa^{WT}, HeLa$^{ATG5\text{-}KO}$, and HeLa$^{VPS35\text{-}KO}$ cells. Scale bar, 10 µm. **I,J.** HCM quantification of GLUT1-SNX27 overlap (% of SNX7 area positive for GLUT1) in HeLa^{WT}, HeLa$^{ATG5\text{-}KO}$, and HeLa$^{VPS35\text{-}KO}$. Scale bar, 20 µm. Data, means ± SE (n=4); one-way ANOVA with Tukey's multiple comparisons. HCM images in all relevant panels, examples from a bank of unbiased operator-independent machine-collected and algorithm-processed fields containing a minimum of 500 primary objects/cells per well (5 wells minimum per 96-well plate; 3 plates minimum), per cell line.

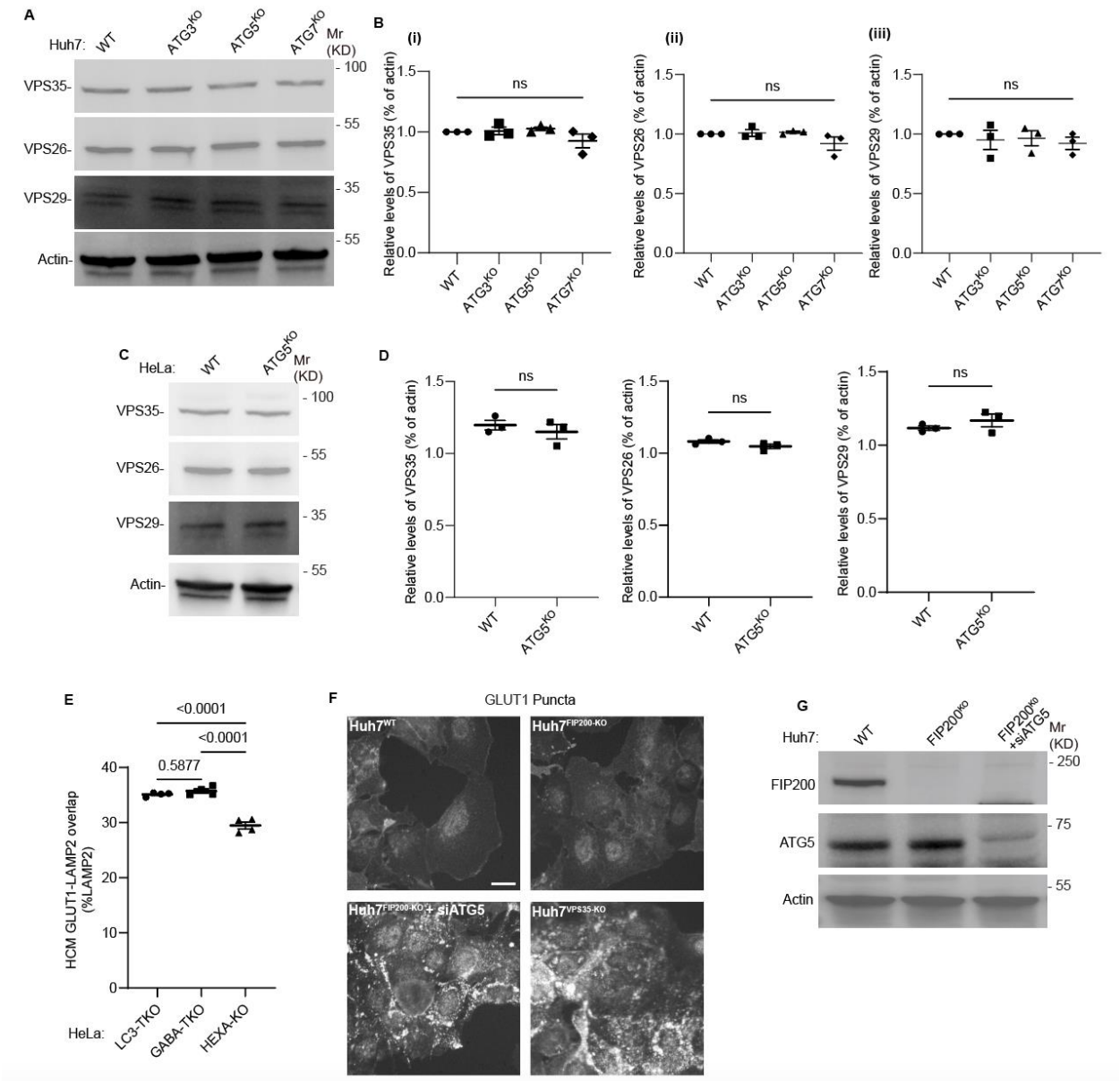

Supplementary Figure S5. ATG5 knockout has no effect on protein levels of retromer subunits. A,B. Immunoblot analysis (A) and quantification (B) of retromer complex proteins VPS35 (i), VPS26 (ii), and VPS29 (iii) from Huh7^{WT}, Huh7$^{ATG3\text{-}KO}$, Huh7$^{ATG5\text{-}KO}$, and Huh7$^{ATG7\text{-}KO}$ cells (total cell extract). **C,D.** Immunoblot analysis (C) and quantification (D) of retromer complex proteins VPS35 (i), VPS26 (ii), and VPS29 (iii) from HeLa^{WT}, and HeLa$^{ATG5\text{-}KO}$ cells (total cell extract). **E.** HCM quantification of GLUT1-LAMP2 colocalization in HeLa$^{LC3\text{-}TKO}$, HeLa$^{GABA\text{-}TKO}$, and HeLa$^{HEXA\text{-}KO}$ cells. Data, means ± SE (n =4), one-way ANOVA with Tukey's multiple comparisons. **F.** HCM images of GLUT1 puncta/cell in Huh7^{WT}, Huh7$^{FIP200\text{-}KO}$, Huh7$^{FIP200\text{-}KO+\ siATG5}$, and Huh7$^{VPS35\text{-}KO}$

cells. **G.** Immunoblot analysis showing the siRNA mediated knockdown of ATG5 in Huh7$^{FIP200\text{-}KO}$ cells. HCM images in panel F, examples from a bank of unbiased operator-independent machine-collected and algorithm-processed fields containing a minimum of 500 primary objects/cells per well (5 wells minimum per 96-well plate; 3 plates minimum), per cell line/condition.

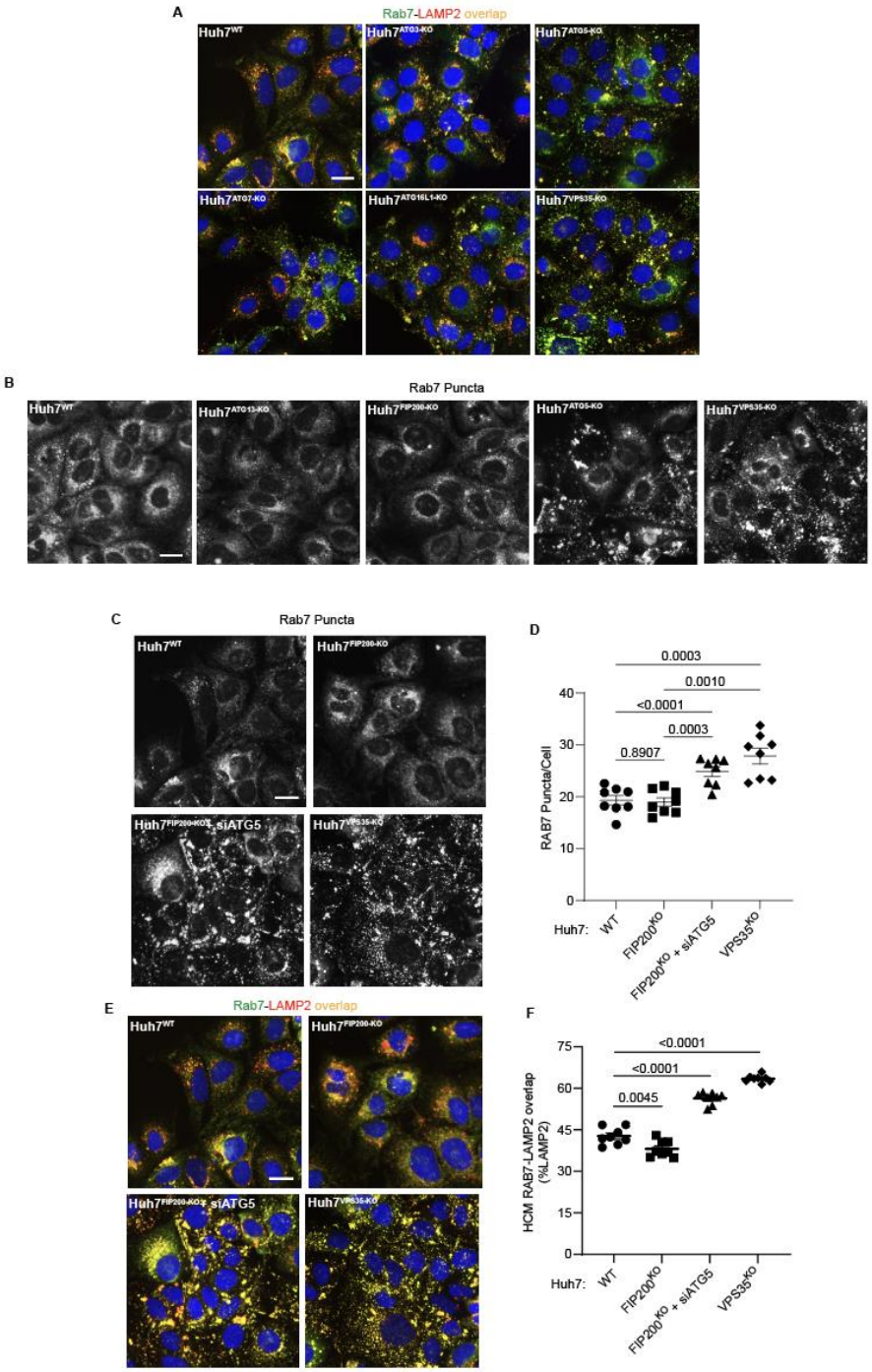

Supplementary Figure S6. Loss of membrane atg8ylation but not of canonical autophagy diverts of RAB7 to lysosomal compartments. A. HCM images of Rab7 (immunostaining of endogenous protein) showing Rab7 colocalization with LAMP2 (% of LAMP2 profiles positive for GLUT1; overlap area) in Huh7^{WT}, Huh7$^{ATG3-KO}$, Huh7^{ATG5-}

^{KO}, Huh7$^{ATG7-KO}$, Huh7$^{ATG16-KO}$, and Huh7$^{VPS35-KO}$ cells. Scale bar, 20 µm. **B.** HCM images of Rab7 (puncta/cell of endogenous Rab7 profiles stained for immunofluorescence) in Huh7^{WT}, Huh7$^{ATG13-KO}$, Huh7$^{FIP200-KO}$, Huh7$^{ATG5-KO}$, and Huh7$^{VPS35-KO}$ cells. Scale bar, 20 µm. **C,D.** HCM images (C) and quantification of RAB7 puncta (D) in Huh7^{WT}, Huh7$^{FIP200-KO}$, Huh7$^{FIP200-KO + siATG5}$, and Huh7$^{VPS35-KO}$ cells. Scale bar, 20 µm. Data, means ± SE (n =8), one-way ANOVA with Tukey's multiple comparisons. **E,F.** HCM images (E) and quantification of RAB7-LAMP2 colocalization (F) in Huh7^{WT}, Huh7$^{FIP200-KO}$, Huh7$^{FIP200-KO + siATG5}$, and Huh7$^{VPS35-KO}$ cells. Scale bar, 20 µm. Data, means ± SE (n =8), one-way ANOVA with Tukey's multiple comparisons. HCM images in all relevant panels, examples from a bank of unbiased operator-independent machine-collected and algorithm-processed fields containing a minimum of 500 primary objects/cells per well (5 wells minimum per 96-well plate; 3 plates minimum), per cell line.

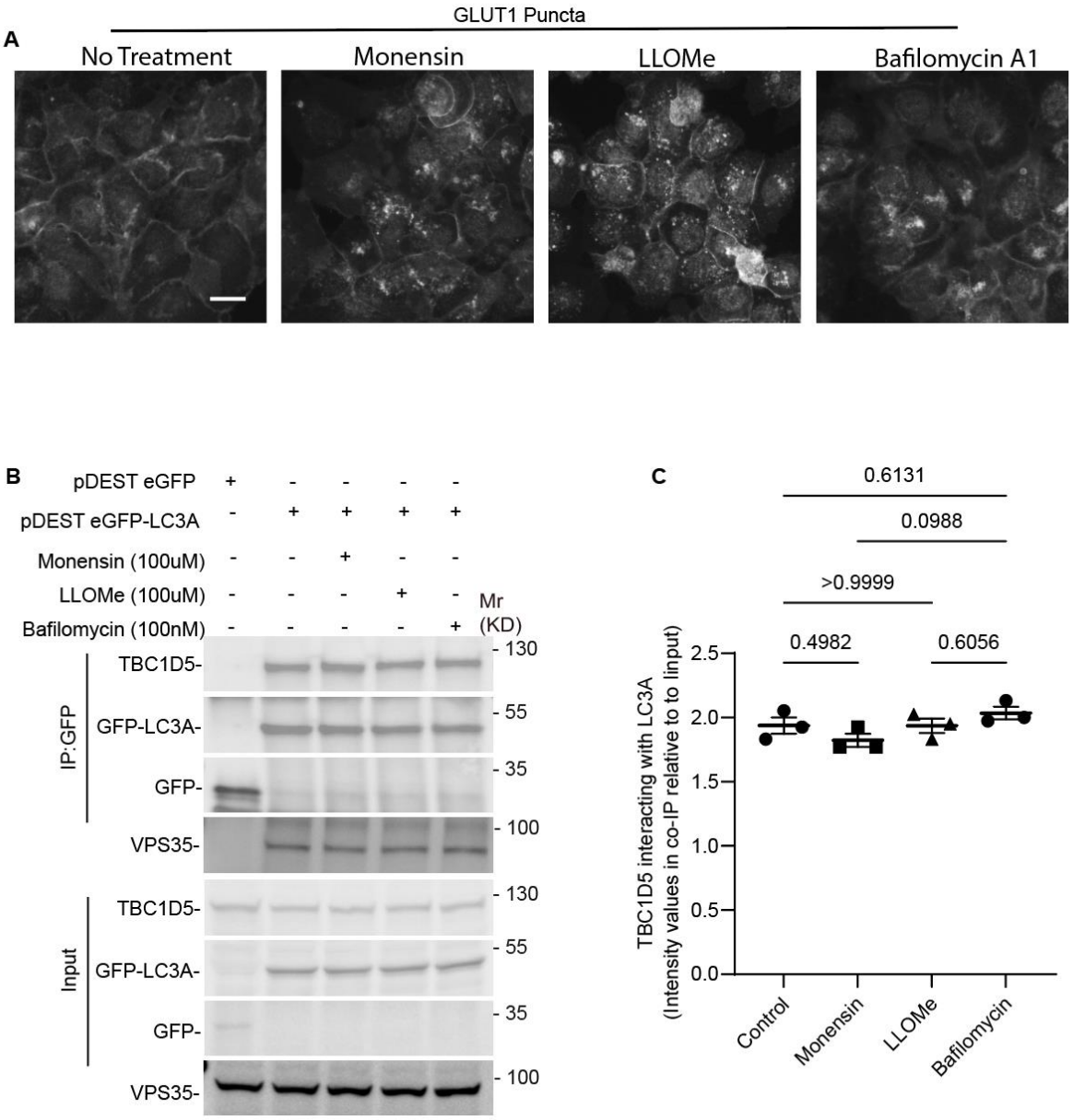

Supplementary Figure S7. CASM agonists effects on retromer cargo GLUT1 in the absence of changes in TBC1D5-LC3A association. A. HCM images of GLUT1 puncta in Huh7^{WT} cells upon treatment with Monensin (100µM), LLOMe (100µM), and Bafilomycin A1 (100nM) for 45 minutes. **B,C.** Co-IP analysis (B) and quantification (C) of TBC1D5 and GFP-LC3 interaction in Huh7 cells treated with or without Monensin (100µM), LLOMe (100µM), and Bafilomycin A1 (100nM) for 45 minutes. Data, means ± SE (n=3), one-way ANOVA with Tukey's multiple comparisons. HCM images in A, examples from a bank of unbiased operator-independent machine-collected and

algorithm-processed fields containing a minimum of 500 primary objects/cells per well (5 wells minimum per 96-well plate; 3 plates minimum), per condition.

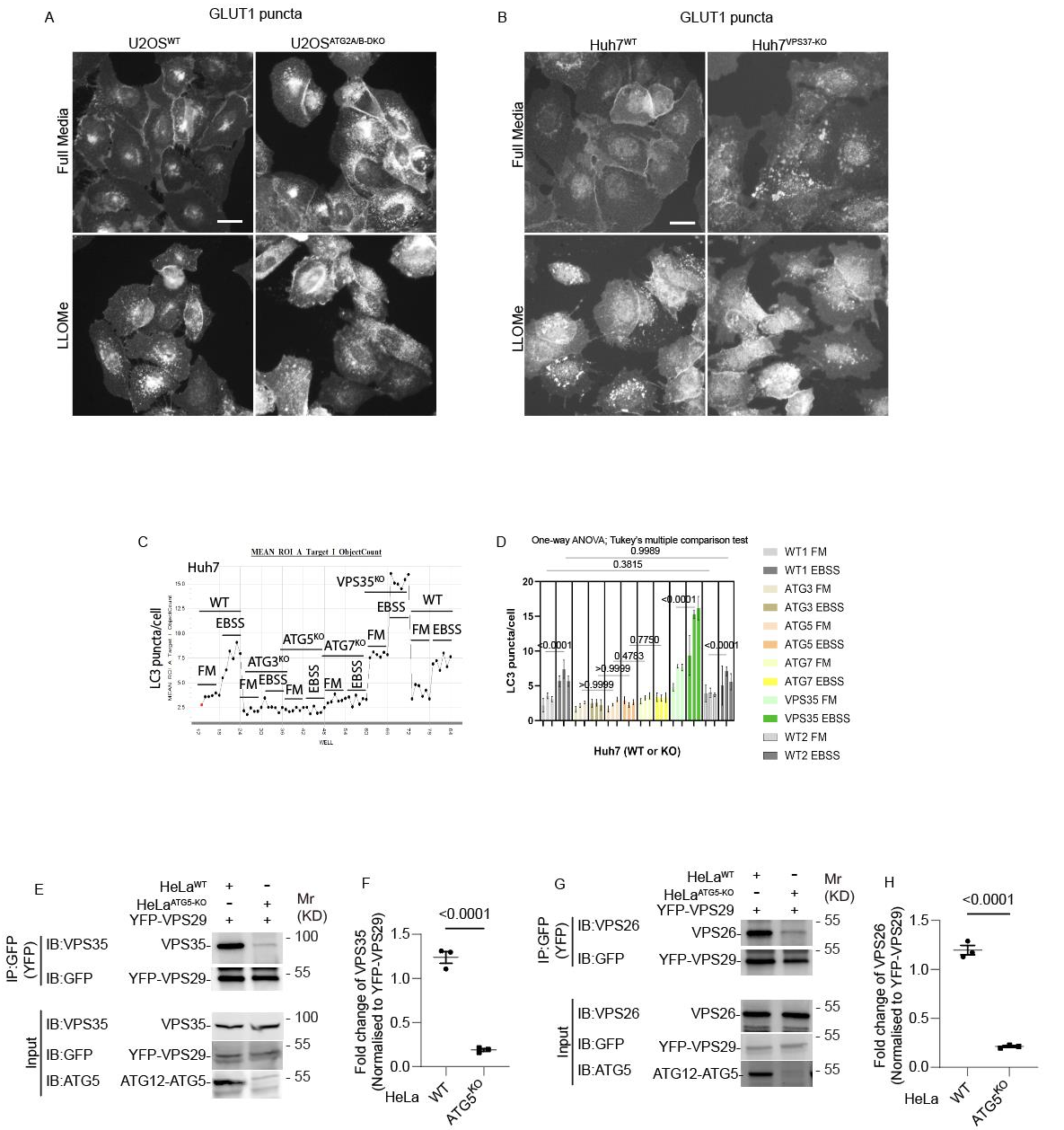

Supplementary Figure S8. **A.** HCM representative images of GLUT1 puncta in U2OS^{WT} and U2OS$^{ATG2A/B-DKO}$ cells upon treatment with LLOMe (100µM) for 45 minutes. **B.** HCM representative images of GLUT1 puncta in Huh7^{WT} and Huh7$^{VPS37A-KO}$ cells upon treatment with LLOMe (100µM) for 45 minutes. **C,D.** HCM quantification of LC3 puncta in Huh7^{WT}, Huh7$^{ATG3-KO}$, Huh7$^{ATG5-KO}$, Huh7$^{ATG7-KO}$, and Huh7$^{VPS35-KO}$ cells induced for autophagy in EBSS for 90 minutes. Plot in C, an example of a whole 96-well plate HCM readout; X axis, well positions; Y axis, HCM parameter quantified. Plot in D, nested data from three different plates each one as in C. FM, full medium; EVSS,

1199 starvation medium. Data, means ± SE (n=3); one-way ANOVA with Tukey's multiple
1200 comparisons. **E,F.** Co-IP analysis (E) and quantification (F) of VPS35 and YFP-VPS29
1201 interaction in HeLa^{WT}, and HeLa$^{ATG5\text{-}KO}$ cells. Data, means ± SE (n=3), one-way ANOVA
1202 with Tukey's multiple comparisons. **G,H.** Co-IP analysis (G) and quantification (H) of
1203 VPS26 and YFP-VPS29 interaction in HeLa^{WT}, and HeLa$^{ATG5\text{-}KO}$ cells. Data, means ±
1204 SE (n=3); unpaired *t*-test.
1205

METHODS

Resource availability

Lead contact

Further information and requests for resources and reagents should be directed to and will be fulfilled by Lead Contact, Vojo Deretic (vderetic@salud.unm.edu).

Materials availability

Plasmids and cell lines generated in this study are available from the lead contact.

Data and code availability

Raw MS DIA/DDA data have been deposited at the MassIVE proteomics repository MassIVE (MSV000090348) and Proteome Exchange (PXD036850).

Any additional information required to reanalyze the data reported in this work paper is available from the Lead Contact upon request.

EXPERIMENTAL MODEL AND SUBJECT DETAILS

Cells and cell line models

HEK293T and HeLa cells were from ATCC (American Type Culture Collection). Huh7 cells were from Rocky Mountain Laboratories.

Mice

Atg5$^{fl/fl}$ LysM-Cre^{-}, Atg5$^{fl/fl}$ LysM-Cre^{+} mice were previously described[Castillo, 2012, 23093667;Manzanillo, 2012, 22607800].

Housing and husbandry conditions of experimental animals

All mice were housed in AAALAC-accredited Animal Research Facility (ARF) of the University of New Mexico Health Sciences Center (UNM-HSC) and institutionally

approved husbandry conditions and approved breeding protocols were followed. *M. tuberculosis*-infected animals were housed in a separate ABSL3 suite within the UNM HSC ARF facility and all staff followed strict ABSL3, BSL3, and animal protocols approved by the UNM HSC Biosafety committee and the Institutional Animal Care and Use Committee. The study was compliant with all relevant ethical guidelines for animal research.

METHOD DETAILS

Antibodies, Reagents and plasmids.

Antibodies from Abcam were ATG5 [1:2000 for Western blot (WB), ab108327], ATG7 (1:2000 for WB, ab52472), GFP [1:2000 for WB; 1:300 for Immunoprecipitation (IP), ab290], mCherry (1:1000 for WB, ab183628), VPS35(1: 500 for WB; 1:1000 for IF, ab10099), VPS29 [1:500 for Immunofluorescence (IF), ab10160], GLUT1 [1:3000 western blot (WB), 1:1000 for Immunofluorescence (IF), ab115730], RAB7 [1:2000 western blot (WB), 1:500 for Immunofluorescence (IF), ab137029].

Antibodies from Biolegend were ALIX [1:400 for Immunofluorescence (IF), #634502], Galectin-3 [1:200 for Immunofluorescence (IF), #125402].

Antibodies from Proteintech were VPS26A [1:500 for Western blot (WB), 12804-1-AP], VPS35 [1:500 for Western blot (WB), 1:1000 for Immunofluorescence (IF), 10236-1-AP], TBC1D5 [1:1000 for Western blot (WB), 17078-1-AP].

Antibodies from Sigma Aldrich were ATG3 [1:1000 for Western blot (WB), #A3231], Ubiquitin [FK2, 1:500 for immunofluorescence (IF), 04-263].

Antibodies from Cell Signaling were α-Tubulin (DM1A) [1:3000 for Western blot (WB); #3873], LAMP1[1:3000 for immunofluorescence (IF), #9091].

Other antibodies used in this study were from the following sources: beta-Actin [1:500 for Western blot (WB), sc-47778] and GAPDH [1:500 for Western blot (WB), sc-47724] from Santa Cruz Biotechnology; LAMP2 [1:1000 for immunofluorescence (IF), H4B4]

from DSHB of University of Iowa; ATG5 [1: 500 for Western blot (WB), ASA-B0113) from Novateinbio, SNX27 [1:1000 for Western blot (WB), MA5-27854] from Invitrogen.

Alexa Fluor 488, 568, 647 [1:500 for immunofluorescence (IF)] and IgG-HRP [1:10000 for western blot (WB)]. Secondary antibodies were from ThermoFisher Scientific. IgG Polyclonal Antibody Goat anti-mouse IRDye 680 (LI-COR, 925-68020), and Goat anti-rabbit IRDye 800 (LI-COR, 926-32211) secondary antibodies were from LI-COR Biosciences.

We also used the following reagents: Bafilomycin A1 (BafA1, InvivoGen; 13D02-MM), Monensin (Sigma, M5273), LLOMe (Sigma, L7393), Lipofectamine 2000 (Thermo Scientific, 11668019); TritonX-100 (OmniPur, 9410-OP), saponin (Sigma, S4521-25G). DMEM (Gibco, #11995040), and Penicillin–Streptomycin (1,000 U/ml; Gibco, #15140122). OptiMEM from Life Technologies, Puromycin dihydrochloride (Sigma, P9620), Hygromycin B (Sigma, H0654)

Plasmids used in this study include eGFP-Rab7 WT (Addgene, #12605), eGFP-Rab7^{Q67L} (Addgene, #28049) and eGFP-Rab7^{T22N} (Addgene, #28049).

Plasmids, siRNAs, and transfection

Plasmids used in this study, such as ATG5 were first cloned into pDONR221 (Gateway Technology cloning vector, Thermo Scientfic) using a BP cloning reaction and the expression vectors were made utilizing LR cloning reaction (Gateway, ThermoFisher) in appropriate (pDEST) destination vectors for immunoprecipitation assay. Plasmid transfections were performed using the Lipofectamine 2000/3000 Transfection Reagent (ThermoFisher Scientific, #11668019).

Cornell model of *M. tuberculosis* latent infection

For this study, a total of 68 mice were used (35 Atg5$^{fl/fl}$ LysM-Cre^{+} and 33 Atg5$^{fl/fl}$ LysM-Cre^{-}). Early in the course of the study, one mouse died due to malocclusion and thus could not be included in the final analysis.

Inoculum was prepared by diluting *M. tuberculosis* Erdman frozen stock 1:50 in PBS/0.01% Tween for a final amount of ~7.38e^6 CFU/mL. Inoculum was serially diluted 5 times at 1:10 each time in PBS/Tween. 50 µL aliquots of the 3rd, 4th, and 5th dilutions were plated on 7H11 agar plates to determine actual inoculum CFUs (Actual inoculum for this study: 6.45e^6 CFU/mL). Remaining inoculum was added to Glas-Col inhalation System and mice were infected via aerosol according to the following machine settings:

Glas-Col Cycle Settings:

M. tuberculosis Erdman diluted 1:50, targeting 200 CFU/mouse.

1. Preheat: (15 minutes)
2. Nebulizing: (20 minutes)
3. Cloud decay: (20 minutes)
4. Decontamination: (15 minutes)- UV lights ON
5. Cool down period: (10 minutes)

Immediately following aerosol infection, 3 C57BL/6 mice, infected in parallel with the experimental cohort, were euthanized to determine lung deposition CFUs. 5 x 200uL aliquots of neat, homogenized tissue were grown for 2-3 weeks at 37°C and 5% CO_2. Initial deposition: ca. 100 CFUs per lung. This procedure was used for all subsequent CFU determinations in this study.

After a period of 2.5 weeks bacterial growth was assessed by determining lung CFUs (2 Cre$^+$ and 1 Cre$^-$ sacrificed)

Subsequently, mice were treated PO with antibiotics (0.1g/L INH and 0.15g/L RIF) in drinking water for 8 weeks and bacterial clearance by chemotherapy was assessed by determining lung CFUs (11 Cre$^+$ and 10 Cre$^-$ sacrificed).

The remaining mice were subjected to antibiotic washout for 7 weeks plus a spontaneous reactivation period with no treatment for 3 weeks at which time lung CFUs were determined (8 Cre$^+$ and 8 Cre$^-$ sacrificed).

After washout and reactivation periods, dexamethasone was administered by IP injection 5 times/week at 0.08mg/mouse/day to induce immunosuppression. Mice were immunosuppressed in this manner for 6 weeks after which point lung CFUs were determined (14 Cre^{+} and 13 Cre^{-} sacrificed).

Generation of CRISPR mutant cells

Knockout cells ($HeLa^{ATG5\text{-}KO}$, $HeLa^{VPS35\text{-}KO}$ $Huh7^{ATG5\text{-}KO}$, $Huh7^{ATG3\text{-}KO}$, $Huh7^{ATG7\text{-}KO}$, $Huh7^{VPS35\text{-}KO}$) were generated by CRISPR/Cas9-mediated knockout system. The lentiviral vector lentiCRISPRv2 carrying both Cas9 enzyme and a gRNA targeting ATG5 (gRNA-puro: AAGAGTAAGTTATTTGACGT), ATG3 (gRNA-Hygro: GTGAAGGCATACCTACCAAC), ATG7 (gRNA-puro: CTTCCGTGACCGTACCATGC), VPS35 (gRNA-hygro: GCTCACCGTGAAGATGGACC), or Scramble (gRNA-hygro: GTGTAGTTCGACCATTCGTG) were transfected into HEK293T cells together with the packaging plasmids psPAX2 and pCMV-VSV-G at the ratio of 5:3:2. Two days after transfection, the supernatant containing lentiviruses was collected. Cells were infected by the lentiviruses with 8-10 µg/mL polybrene. 36 h after infection, the cells were selected with puromycin (1-10 µg/mL) or hygromycin (100-500 µg/ml) for one week in order to select knockout cells. All knockouts were confirmed by western blot. Selection of single clones was performed by dilution in 96-well.

High content microscopy (HCM)

Cells in 96 well plates were fixed in 4% paraformaldehyde for 5 min. Cells were then permeabilized with 0.1% saponin in 3% Bovine serum albumin (BSA) for 30 min followed by incubation with primary antibodies for 2 h and secondary antibodies for 1h. Hoechst 33342 staining was performed for 3 min. High content microscopy with automated image acquisition and quantification was carried out using a Cellomics HCS scanner and iDEV software (ThermoFisher Scientific). Automated epifluorescence image collection was performed for a minimum of 500 cells per well. Epifluorescence images were machine analyzed using preset scanning parameters and object mask definitions. Hoechst 33342 staining was used for autofocusing and to automatically define cellular outlines based on background staining of the cytoplasm. Primary objects

were cells, and regions of interest (ROI) or targets were algorithm-defined by shape/segmentation, maximum/minimum average intensity, total area and total intensity, etc., to automatically identify puncta or other profiles within valid primary objects. Each experiment (independent biological repeats; n≥3) consists of machine-identified 500 valid primary objects/cells per well, ≥5 wells/sample. All data collection, processing (object, ROI, and target mask assignments) and analyses were computer driven independently of human operators. HCM also provides a continuous variable statistic since it does nor rely on parametric reporting cells as positive or negative for a certain marker above or below a puncta number threshold.

Co-IP and immunoblotting assays

For co-IP, cells transfected with 8–10 μg of plasmids were lysed in ice-cold NP-40 buffer (Thermo Fisher Scientific) supplemented with protease inhibitor cocktail (11697498001; Roche) and 1 mM PMSF (93482; Sigma-Aldrich) for 30 min on ice. Lysates were centrifuged for 10 min at 10,000 g at 4°C. Supernatants were incubated with (2–3 μg) antibodies overnight at 4°C. The immune complexes were captured with Dynabeads (Thermo Fisher Scientific), followed by three times washing with 1 x PBS. Proteins bound to Dynabeads were eluted with 2 x Laemmli sample buffer (Bio-Rad) and subjected to immunoblot analysis.

For immunoblotting, lysates were centrifuged for 10 min at 10,000× g at 4°C. Supernatants were then separated on 4–20% Mini-PROTEAN TGX Precast Protein Gels (Biorad) and transferred to nitrocellulose membranes. Membranes were blocked in 3% BSA for 1 h at RT and incubated overnight at 4°C with primary antibodies diluted in blocking buffer. They were then incubated with an HRP-conjugated secondary antibody, and proteins were detected using ECL and developed using ChemiDoc Imaging System (Biorad). Analysis and quantification of bands were performed using ImageJ software.

LysoIP assay:

Plasmids for LysoIP were purchased from Addgene. Cells were plated in 10 cm dishes in DMEM and 10% FBS and transfected with pLJC5-TMEM192-3xHA or pLJC5-TMEM192-2XFLAG constructs at 75-85% confluency. After 24 hours of transfection, cells with or without treatment were quickly rinsed twice with PBS and then scraped in

1mL of KPBS (136 mM KCl, 10 mM KH_2PO_4, pH7.25 adjusted with KOH) and centrifuged at 3000 rpm for 2 min at 4^0C. Pelleted cells were resuspended in 1000 µL KPBS and reserved 50 µL for further processing of the whole cell. lysate. The remaining cells were gently homogenized with 20 strokes of a 2 mL homogenizer. The homogenate was then centrifuged at 3000 rpm for 2 min at 4 ^{0}C and the supernatant was incubated with 100 µL of KPBS prewashed anti-HA magnetic beads (ThermoFisher) on a gentle rotator shaker for 15 min. Immunoprecipitants were then gently washed three times with KPBS and eluted with 2 x Laemmli sample buffer (Bio-Rad) and subjected to immunoblot analysis.

Immunofluorescence confocal microscopy and analysis

Cells were plated onto coverslips in 6-well plates. After treatment, cells were fixed in 4% paraformaldehyde for 5 min followed by permeabilization with 0.1% saponin in 3% BSA for 30 min. Cells were then incubated with primary antibodies for 2 h and appropriate secondary antibodies Alexa Fluor 488 or 568 (ThermoFisher Scientific) for 1 h at room temperature. Coverslips were mounted using Prolong Gold Antifade Mountant (ThermoFisher Scientific). Images were acquired using a confocal microscope (META; Carl Zeiss) equipped with a 63 3/1.4 NA oil objective, camera (LSM META; Carl Zeiss), and AIM software (Carl Zeiss).

Sample preparation for LC-MS/MS

The previously described HeLaFp-In-APEX2-ATG5-WT and HeLaFlp-InAPEX2-ATG5-K130R cells [Wang, 2023, 37054706] were incubated in complete medium supplemented with 500 µM biotin–phenol (AdipoGen) with or without 2 mM LLOMe for 30 min. A 1-min pulse with 1 mM H_2O_2 at room temperature was stopped with quenching buffer (10 mM sodium ascorbate, 10 mM sodium azide and 5 mM Trolox in PBS). All samples were washed twice with quenching buffer, and twice with PBS for 1 min. For LC–MS/MS analysis, cell pellets were lysed in 500 µl ice-cold lysis buffer (6 M urea, 0.3 M NaCl, 1 mM EDTA, 1 mM EGTA, 10 mM sodium ascorbate, 10 mM sodium azide, 5 mM Trolox, 1% glycerol and 25 mm Tris-HCl, pH 7.5) for 30 min by gentle pipetting. Lysates were clarified by centrifugation and protein concentrations were determined using Pierce 660 nm protein assay reagent. Streptavidin-coated magnetic beads (Pierce) were washed with lysis buffer. A total of 1 mg of each sample was mixed

with 100 µl of streptavidin beads. The suspensions were gently rotated at 4 °C overnight to bind biotinylated proteins. The flow-through after enrichment was removed and the beads were washed in sequence with 1 ml IP buffer (150 mM NaCl, 10 mM Tris-HCl, pH 8.0, 1 mM EDTA, 1 mM EGTA, 1% Triton X-100) twice; 1 ml 1 M KCl; 1 ml of 50 mM Na2CO3; 1 ml 2 M urea in 20 mM Tris HCl (pH 8.0); and 1 ml IP buffer. Biotinylated proteins were eluted and processed for mass spectrometry. Protein samples on magnetic beads were washed four times with 200 µl of 50 mM Triethyl ammonium bicarbonate (TEAB) with a twenty-minute shake time at 4 °C in between each wash. Roughly 2.5 µg of trypsin was added to the bead and TEAB mixture and the samples were digested over night at 800 rpm shake speed. After overnight digestion the supernatant was removed, and the beads were washed once with enough 50 mM ammonium bicarbonate to cover. After 20 min at a gentle shake the wash is removed and combined with the initial supernatant. The peptide extracts are reduced in volume by vacuum centrifugation and a small portion of the extract is used for fluorometric peptide quantification (Thermo scientific Pierce). One microgram of sample based on the fluorometric peptide assay was loaded for each LC-MS analysis.

Liquid chromatography-tandem mass spectrometry

Peptides were desalted and trapped on a Thermo PepMap trap and separated on an Easy-spray 100 µm × 25 cm C18 column using a Dionex Ultimate 3,000 nUPLC at 200 nL/min. Solvent A = 0.1% formic acid, Solvent B = 100% Acetonitrile 0.1% formic acid. Gradient conditions = 2% B to 50% B over 60 min, followed by a 50%–99% B in 6 min and then held for 3 min than 99% B to 2% B in 2 min and total run time of 90 min using Thermo Scientific Fusion Lumos mass spectrometer. The samples were run in DIA mode; mass spectra were acquired using a collision energy of 35, resolution of 30 K, maximum inject time of 54 *ms* and an AGC target of 50K, using staggered isolation windows of 12 Da in the *m/z* range 400–1,000 *m/z*.

DIA Quantification and Statistical Analysis

DIA data was analyzed using Spectronaut 14.10 (Biognosys Schlieren, Switzerland) using the directDIA workflow with the default settings. Briefly, protein sequences were

downloaded from Uniprot (Human Proteome UP000005640), ATG5 from Uniprot and common laboratory contaminant sequences from https://thegpm.org/crap/. Trypsin/P specific was set for the enzyme allowing two missed cleavages. Fixed Modifications were set for Carbamidomethyl, and variable modification were set to Acetyl (Protein N-term) and Oxidation. For DIA search identification, PSM and Protein Group FDR was set at 1%. A minimum of 2 peptides per protein group were required for quantification. Proteins known to be endogenously biotinylated were excluded from consideration.

Quantification and statistical analysis

Data in this study are presented as means ± SEM (n ≥ 3). Data were analyzed with either analysis of variance (ANOVA) with Tukey's HSD post-hoc test, or a two-tailed Student's t-test. For HCM, n ≥ 3 is included in each independent experiment: ≥500 valid primary objects/cells per well, from ≥ 5 wells per plate per sample. Statistical significance was defined as: ns (not significant) or <0.05 (significant). For HCM, sample size was based on a historic power analysis (published studies), with large effect size (differences and variability derived from published work), power 80%, β 20%, and α 5%, assuming normal distribution and favoring type II false negative errors over type I false positive errors. Band intensity in immunoblots, n=3 (biological replicates); no power analysis was performed.